Contents

J Indian Inst. Sci., Sept.–Oct 1994, 74, 649–713

IISc THESES ABSTRACTS

Thesis Abstract (M.Sc. (Engng))

Instruction scheduling for RISC processors by R. Venugopal

Research supervisor: Y. N. Srikant
Department: Computer Science and Automation

1. Introduction

Instruction scheduling is an important feature in the code generation phase of a high-performance reduced instruction set computer (RISC) compiler. It is the process of reordering instructions (whether assembly code or code in some other form) so as to make fuller use of the resources provided by the RISC processor. The resources include pipelines, multiple functional units, a large register set, delayed branching, delayed loading, instruction chaining, etc.

The most common approach to the instruction scheduling problem is to build a weighted, directed graph which reflects the dependency relations. In this case, the nodes of the graph represent the instructions and the edges between them represent the dependency constraints. The weights on the edges connecting the nodes represent the latency times between the instructions represented by these nodes. Such a graph is called a dependency-directed acyclic graph (DAG) On this dependency DAG, some form of prioritized sorting of the nodes is done to get a modified schedule of instructions. This modified schedule will hopefully make better use of the resources provided by the RISC processor. The works of Hennessey and Gross[1], Gibbson and Muchnick[2] & Palem and Simon[3] give different solutions to various instruction scheduling problems.

Most problems in this area are NP-complete. Hence there are two distinct paradigms for tackling them. The first approach is to design heuristic solutions to the problem which do not necessary produce optimal schedules but produce reasonably good code. The second approach is to design optimal solutions to restricted versions of the problem which are, however, still useful in practice.

In this work, we have looked at two different instruction scheduling problems. The first problem deals with the generation of code with instruction chaining from DAGs. We adopt the first paradigm of solving the problem heuristically. The second problem deals with generating optimal code from expression trees which have register variables. The code is generated for what are called delayed load architectures. For this problem, we adopt the second paradigm of getting an optimal solution to a restricted version of the problem.

2. Chaining in DAGs

Instruction chaining is a feature possessed by vector processors like the Cray-1, the Cray X-MP and the Fujitsu VP-200 It is also present in a slightly modified form in the RISC processor, Intel i860

Two instructions can be chained together if they are processed by different functional units and the results register of the first instruction is used as the source register of the second instruction with all other registers being different. Chained instructions are assumed to take up only one time unit. Hence the objective is to design an algorithm which optimizes the code by maximizing chaining with the given number of registers.

An optimal algorithm for this problem exists for expression trees[4]. For DAGs the problem is NP-complete. Therefore, we have designed a heuristic for this problem. It is a greedy heuristic which schedules the longer chains as far as possible. Register allocation is by usage counts[5].

This simple heuristic was implemented and tested for large DAGs. Its performance was compared with other methods. In each case the greedy heuristic was found to outperform the other methods especially when the number of registers was large. An extension to the heuristic which splits the original DAG into a number of smaller sub-DAGs was also considered. The extension further improved the performance but at increased computational cost.

3. Scheduling for delayed load architectures

Our second problem looks at instruction scheduling for delayed load architectures. In a delayed load architecture, the contents of a register being loaded can be accessed only after a certain latency period has elapsed. In our case we considered unit latency times. If an attempt is made to access the contents of the register before the elapsing of the latency period, then a pipeline interlock is caused. It is the responsibility of the instruction scheduler to order the instructions in such a way that the number of interlocks is minimized. This machine model is an approximation of the integer functional units of the SPARC and MIPS R3000 processors.

A simple linear-time, optimal algorithm for this problem exists[6]. This algorithm works on expression trees. But it has the restriction that all the leaves in the tree can refer only to memory locations. They cannot be register variables. In our work, we have generalized this algorithm in such a way that register variables are permitted. Register variables are important in code generation across basic blocks, code generation from DAGs and when there is a global register allocator. Like the earlier algorithm, our algorithm integrates register allocation with instruction scheduling thus optimizing the register usage. It is also linear time and an extension to it incorporates optimal spilling.

For tackling this problem, we define three transformations on the expression tree. We then prove the equivalence of the optimal code sequence of the original tree and that for the transformed tree. We derived three conditions for the optimum usage of registers. These three conditions also give the optimal order of evaluation of the tree. Our algorithm uses these conditions in generating the code. Finally, we prove the optimality of the algorithm.

The algorithm acts as a good heuristic for architectures with longer latency times and in code generation from DAGs.

4. Conclusion

In this thesis, we have looked at two different instruction scheduling problems. We have designed a heuristic solution for the first problem which is shown to work well in practice. For the second problem we have devised an optimal algorithm. The optimality of this algorithm is proved formally.

References

1. HENNESSAY, J. L. AND GROSS, T. — Postpass code optimization of pipeline constraints, *ACM Trans. Progrm. Lang. Syst.*, 1983, **5**, 442–448.
2. GIBBONS, P. B. AND MUCHNICK, S. S. — Efficient instruction scheduling for a pipelined architecture. In *Proc. SIGPLAN '86 Symp. on Compiler Construction*, pp. 11–16, June 1986.
3. PALEM, K. V. AND SIMONS, B. — Scheduling time-critical instruction on RISC machines. In *Proc. ACM Symposium on Principles of Programming Languages*, 1990.
4. BERNSTEIN, D., BORAL, H. AND PINTER, R. Y. — Optimal chaining in expression trees, *IEEE Trans.*, 1988, **C-37**, 1366–1374.
5. FREIBURGHOUSE, R. A. — Register allocation via usage counts, *Commun. ACM*, 1974, **17**, 638–642.

Thesis Abstract (Ph.D.)

Metal–silicate fractionation in the primitive solar nebula: A computational study of the role of $f(O_2)$, P T and charged species by Suhrita Bagchi

Research supervisors: G. V. Anantha Iyer, A. G. Menon and M. Subba Rao
Department: Inorganic and Physical Chemistry

1. Introduction

The results of computational studies of the physico-chemical conditions associated with the condensation of high-temperature phases within the primitive solar nebula are presented. The focus of these studies is on understanding the effect of two compositional parameters within the nebula gas which brought about large separation in the condensation temperatures of metal (represented here by the Fe–Ni–Si alloy) and silicates. The two compositional factors chosen are: (a) the abundance of oxygen and (b) the presence of charged species within the primordial nebula. The studies have been carried out using the program SOLGASMIX[1, 2] which utilizes the method of steepest descent for minimizing the free energy of a system consisting of a gas phase, liquid and solid solutions and stoichiometric phases for a fixed pressure, temperature and system composition.

2. Metal–silicate fractionation

To investigate the condensation behaviour of solids in oxidising and reducing environments a systemic study has been carried out by varying the amount of oxygen in the input data of SOLGASMIX between 12.0 and 24.0 moles[3, 4] (which corresponds to a variation in the C/O ratio between 1.0 and 0.5). The effect of variation in the input amount of oxygen on the fugacities of important gaseous species in the H–O–C–N system (H_2, CO, N_2, CH_4, H_2O, NHJ3 and CO_2) reveals an important aspect of the distribution of oxygen in the equilibrium assemblage. It is seen that oxygen preferentially attaches itself to C to form CO, and since carbon monoxide consumes more than 95% of O, the availability of oxygen for stabilizing other oxygen-bearing species sharply decreases under low $f(O_2)$ conditions. This has an interesting consequence on the condensation temperatures of the first formed silicate, olivine, and the Fe–Ni–Si alloy. The condensation temperature of olivine goes down from 1448 K for computations with 24 0 moles of oxygen to 1152 K when only 12.0 moles of oxygen are included. The Fe–Ni–Si alloy's condensation temperature, however, remains remarkably constant throughout the range of input amount of oxygen, at 1470 K, except under extreme reducing conditions where it rises sharply to 1613 K. Figure 1 is a plot of log $f(O_2)$ *versus* temperature for the first appearance of Fe–Ni–Si and olivine. Thus, it can be seen from the figure that the difference in the stabilization temperatures of these two phases at a pressure of 10^{-3} bar varies from 22 K (24 moles oxygen) through 37 K (20.1 moles), 49 K (18 moles), 81 K (15 moles) to 461 K (12 moles). The log $f(O_2)$ stability range for olivine varies from –30.8 to –16 9 and for the Fe–N–Si alloy the variation is in the range of –26.9 to –16 6.

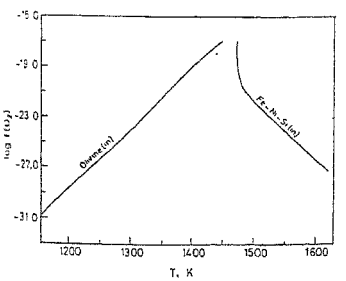

Fig 1. log $f(O_2)$ *versus* temperature plot for the first appearance of Fe–Ni–Si and olivine.

Computations under extreme reducing conditions also indicated a reversal of the condensation sequence between corundum (the first formed phase under 'normal' oxidation conditions) and Fe–Ni–Si with the alloy condensing before corundum under low $f(O_2)$ conditions. Additionally, a new phase Fe–Ni carbide solid solution, becomes the first phase to condense in low $f(O_2)$ environments. The P–T stability fields of the high

temperature condensates under extreme reducing conditions also show the overall depression in the condensation temperatures of the oxide and silicate phases and an increase in the Fe–Ni–Si condensation temperature in the P–T range of 1100 to 2000 K and 1 to 10^{-3} bar, respectively.

3. Charged species

Based on the suggestion of Alfven[5] and Arrhenius[6] of the role of charged species in the primitive solar nebula three sets of computations have been carried out to articulate the abundance, composition and consequence of the presence of charged species in the condensation of high-temperature phases in the primitive nebula. The charged species included in the computation are. (a) oxygen-bearing species (O^-, O_2^-, O^+,O_2^+), (b) species in the H–O–C–N system (C^*, C^-, H^+, H^-, H_2^+, H_2^-, N_2^+, N_2^-, N^+, N^-, CO_2^-, C_2^-, NO^+, CN^+, CN^-, HO, HO^+, CH^+, NO_2 and N_2O^+), and (c) species in the Al–O system (O^-, O^+, O_2^-, O_2^+, Al^+, AlO^+, Al_2O^+, $Al_2O_2^+$, $AlOH^+$, AlO^-, AlO_2^-, $AlOH_2^+$). The P–T range for the oxygen study was 10^{-6} to 10^{-3} bar and 1500 to 2000 K; for the H–O–C–N system study 10^{-2} to 10^{-4} bar and 1300 to 1650 K; and for the Al–O system 10^{-5} to 10^{-1} bar and 1110 to 1950 K. No attempt has been made to include charge balance in these computations

In general, gaseous charged species are seen to be stable in the computed equilibrium assemblage with the negatively charged species being preponderant In the first set of computations involving oxygen-charged species, for instance, the abundance was in the order $O^- > O > O_2^- > O_2 > O_2^+ > O^+$. Charged species in the H–O–C–N system further indicated that their presence had an effect in modifying the condensation behaviour of the first-formed solid phases. Thus, at 10^{-3} bar, the condensation temperature of Fe–Ni–Si increased by 63 K whereas that of melilite, spinel, olivine and clinopyroxene decreased by 68, 46, 47 and 6 K, respectively, when compared to the condensation temperatures in computations without charged species. This resulted in an increase in the difference between the Fe–Ni–Si and olivine condensation temperature from 37 K in a neutral gas to 147 K when charged species were considered.

The computations in the Al–O system brought out yet another consequence of the presence of charged species in the condensation process. Since the Al-bearing gaseous charged species are quite stable, they retain most of the input amount of aluminium in the gas phase. The result is that the aluminious minerals such as corundum, gehlenite and spinel come out at much lower temperatures. This happens principally because at both lower temperatures and higher pressures the importance of charged species diminishes (as is seen in the reduction of their fugacities) and the condensation pattern of the various phases becomes identical to the computations when no charged species were considered.

References

1. ERIKSSON, G. — Thermodynamic studies of high temperature equilibria. XII SOLGASMIX, a computer program for calculation of equilibrium composition in multiphase systems, *Chem. Scr.*, 1975, **8**, 100–103.
2. SAXENA, S. K. AND ERIKSSON, G. — Chemistry of the formation of the terrestrial planets. In *Advances in physical geochemistry*, Vol. 6, 1986 (Saxena, S. K., ed.), pp. 30–105, Springer.
3. ANDERS, E. AND EBIHARA, M. — Solar system abundances of elements, *Geochim. Cosmochim. Acta*, 1982, **46**, 2363–2380.
4. GREVESSE, N. AND ANDERS, E. — Solar system abundances of the elements: A new table. In *Cosmic abundances of matter* (C. J. Waddington, ed.), American Institute of Physics Conference Proceedings, 183, 1989, pp. 1–8, AIP, New York.
5. ALFVEN, H. — *Cosmic plasma*, Astrophysics and Space Science Library, Vol. 82, p. 164, 1981, D. Reidel.
6. ARRHENIUS, G. — Chemical aspects of the formation of the solar system. In *The origin of the solar system* (S. F. Dermott, ed.), pp. 521–581, 1978, Wiley.

Thesis Abstract (M. Sc. (Engng))

Investigations of supported catalysts by *in-situ* Mössbauer spectroscopy and allied techniques by K. R. Kannan

Research supervisor: C. N. R. Rao
Department: Materials Research Centre

1. Introduction

Heterogeneous catalysts constitute a vital branch of chemistry and chemical technology. Supported metal catalysts are not only employed in the chemical industry but are also used in environmental protection, their applications being as diverse as petroleum reforming, fat hardening, and the treatment of vehicle exhaust

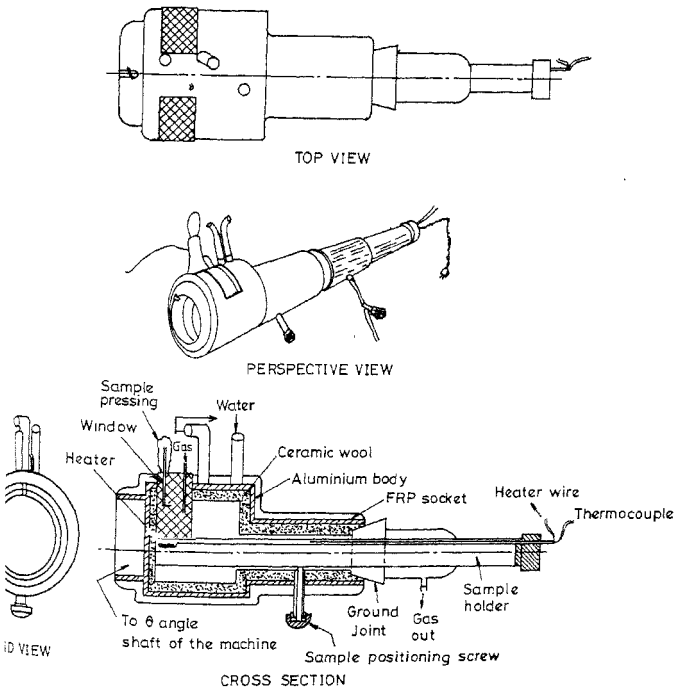

Fig. 1. End, cut and perspective views of the high-temperature *in-situ* cell for XRD.

emission. Traditionally these catalysts have been designed based on trial and error as well as empirical rules. The structural information about the catalysts as well as the species responsible for activity and selectivity are not well established. In this work some of the mono- and bimetallic catalysts used for various reactions[1-3] have been investigated.

2. Experimental

Mössbauer spectroscopy is an excellent technique to investigate iron-containing catalysts, as the catalysts can be studied in the gaseous environments in which they are active. A microprocessor-based Mössbauer spectrometer, with battery back up was designed and fabricated. A least square Lorentzian curve fitting programme was used in Vax88 computer for analysing the Mössbauer spectra.

For both Mössbauer and EXAFS, a cell to record spectrum in the *in-situ* conditions in the transmission geometry was designed and fabricated. For XRD, another *in-situ* cell in reflection geometry was designed and fabricated (Fig. 1). In the XRD cell patterns could be recorded at high temperatures. Both the cells were of low cost with indigeneous materials.

Catalyst samples were prepared using both wet impregnation and precipitation techniques.

3. Summary of important results

3.1. *Fe/TiO₂*

Based on *in-situ* Mössbauer and X-ray diffraction studies, it is shown that in the Fe/TiO_2 catalyst, the anatase–rutile transformation of the TiO_2 support is facilitated by the Fe^{2+} ions formed during reduction. The transformation of anatase to rutile seems to occur at or below the temperature (~770 K) at which strong metal-support interaction manifests itself.

3.2. *Fe/Al₂O₃*

It is possible that metal-support interaction occurs in Fe/Al_2O_3 catalyst reduced at high temperature ($\geq$ 1200 K). This would probably involve the reduction of the aluminate ($FeAl_2O_4$), formed initially by the interaction of the impregnated transition metal ions with the γ-Al_2O_3 support) to give the reduced iron metal and α-Al_2O. The occurrence of such a γ–α transformation of Al_2O_3 could be of some significance just as the anatase-rutile transformation of TiO_2.

3.3. *Fe/SiO₂*

In the dried Fe/SiO_2 precursor, iron interacts strongly with the SiO_2 support forming a ferrous silicate phase reduction to the metallic state not being more than 20% even after reduction at 1023 K. If the catalyst reduced at 723 K is exposed to air at room temperature, it completely converts back to Fe^{3+}. This is an example of the $Fe^{+} \leftrightarrow Fe^{3+}$ oxidation–reduction involving metal-support interaction. In Fe/SiO_2, calcined at 723 K and then reduced at 723 K catalyst, more than 50% of the Fe^{3+} remains unreduced.

3.4. *Ni/SiO₂*

In Ni/SiO_2 catalysts, reduced at 723 K, only 50% of the nickel is reduced to the matallic state. When the Ni/SiO_2 precursor dried at 350 K was calcined at 723 K and then reduced at 723 K almost all the nickel gets reduced to metal.

3.5. *Fe–Ni/SiO₂*

Under similar conditions of preparation, monometallic Fe/SiO_2 and Ni/SiO_2 catalysts at best show partial reduction of the transition metal ions to the metallic state on treatment with hydrogen at 723 K. The maximum reduction to the metallic state in the case of the Fe/SiO_2 catalyst is 20% while it is 50% in the Ni/SiO_2 catalyst. In bimetallic $Fe–Ni/SiO_2$ catalysts (Fig. 2), there is mutual promotion of the two metals towards reduction. The reduction of nickel is nearly complete in all the compositions whereas the reduction of iron is maximum (up to 85%) in the Fe(50)–Ni(50) catalyst. The structural and magnetic properties of the reduced Fe–Ni catalysts vary

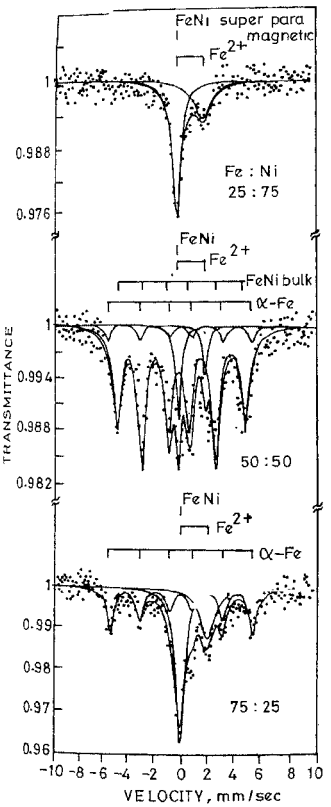

Fig. 2. Mössbauer spectra of Fe–Ni/SiO_2 catalysts dried at 350 K and then reduced at 723 K with different Fe-Ni ratios.

with the composition as well as with the temperature of calcination. The general result is that in Ni-rich compositions, Fe(25)–Ni(75), a superparamagnetic alloy is formed, the structure of which is either BCC or FCC depending on the temperature of calcination. In the Fe-rich compositions, Fe(75)–Ni(25), α-Fe occurs

along with a mixture of superparamagnetic and ferromagnetic alloy phases. In the Fe(50)–Ni(50) composition an FCC ferromagnetic alloy is the predominant species. The composition of the most active Fe–Ni catalyst is known to be Fe(25)–Ni(75); this composition would mainly comprise small superparamagnetic alloy particles of FCC structure. The increased reducibility in the Fe–Ni bimetallic system is clearly related to the facility with which Fe and Ni can form alloy phases. The present study has not only unravelled novel magnetic and structural features of the Fe–Ni bimetallic catalysts, but has also shown how the reducibility and associated performance are related to the facility of alloy formation by the two component transition metals on the surface of the catalysts.

3.6. *Fe–Ru/SiO_2, Fe–Ru/Al_2O_3 and Fe–Ru/TiO_2*

When the relative proportion of Ru in the Fe–Ru/SiO_2 catalysts is small, the observed enhancement in the reducibility of iron is mainly due to the hydrogen spillover process. The reduction leads to the formation of Fe^{2+} or Fe^0 depending on the reduction temperature. The reduction of iron in Fe–Ru/SiO_2 catalysts to the metallic state is promoted by FeRu alloy formation. The alloy formation and the reducibility of iron increase with the increase in the Ru content. Reduction at 523 K of the Fe(5)–Ru(1)/SiO_2 catalyst shows the presence of Fe^{2+} (~25%), Fe^{3+} (~25%) and FeRu alloy (~5%). With increase in the Ru content, the proportion of Fe^{3+} decreases by a simultaneous increase in the FeRu alloy phase, the proportion of Fe^{2+} is nearly constant. However, when the reduction is carried out at 723 K, most of the iron in the Ru-rich compositions is present in the form of FeRu alloy. When Ru/Fe ≥ 1.0, there is neither Fe^{2+} nor any segregated α-Fe and the proportion of Fe^{3+} is also low. A reduction temperature of 723 K should therefore be employed for this bimetallic catalysts.

The Fe^{3+} species often found in reduced Fe–Ru/SiO_2 catalysts is probably due to the oxidation of fine Fe particles formed on the support.

A comparative study with different supports has shown that the SiO_2 and γ-Al_2O_3 supports interact with iron in the Fe–Ru catalyst during the reduction at 523 K and form the silicate and the aluminate phases, respectively. A higher reduction temperature of 723 K, however, reduces the Fe^{2+} phase to the FeRu alloy. On the other hand, the TiO_2 support remains inert at low temperatures of reduction and interacts only at higher temperatures (> 723 K) forming a titanate.

References

1. TAU, L. M. AND BENNET, C. L. — Kinetic and Mossbauer study of the CO/H_2 reaction over Fe/TiO reduced at various temperatures, *J. Catal.*, 1984, **89**, 285–302.
2. MATUYAMA, M., ASHIDA, K., TAKAYASU, O. AND TAKEUCHI, T. — Catalytic activities of Ni alloys expressed by surface and bulk compositions., *J. Catal.*, 1986, **102**, 309–315.
3. NIEMANTSVERDRIET, J. W., VANKAAM, A. C., FLIPSE, C. F. J. AND VAN DER KRAAN, A. M. — Supported bi-metallic catalysts, *J. Catal.*, 1985, **96**, 58–71.

Thesis Abstract (Ph.D.)

Low-temperature synthesis and characterization of fine particle Perovskite oxides and structurally related mixed metal oxides: Studies on zirconates, titanates and cuprates by M. Rajendran

Research supervisor: M. Subba Rao
Department: Inorganic and Physical Chemistry

1. Introduction

The members of the Perovskite and structurally related oxide families exhibit interesting electrical, magnetic and superconducting properties which are of tremendous technological importance. The properties of these

oxides depend to a large extent on the method of preparation and processing conditions. The conventional methods of ceramic preparation lead to the products, lacking in purity, action stoichiometry and desired powder characteristics. These factors significantly affect the physical properties of the sintered compacts. Hence the development of innovative synthetic methods and processing strategies have attracted considerable interest in recent years. Among the various methods carboxylate complexation is one of the simple, convenient and efficient synthesis routes[1–3].

In the present investigation a series of simple and mixed metal citrate and tartrate complexes have been prepared and thermally decomposed to produce monophasic, submicron oxide powders at relatively low temperatures and short durations of heating.

2. Experimental

The following simple and mixed metal citrate and tartrate complexes have been prepared under optimized conditions: $NH_4[ZrO(C_6H_5O_7)]2H_2O$ (AZC), $H[ZrO(C_6H_5O_7)]\ 2H_2O$ (HZC), $(ZrO_3)[C_6H_5O_7]_2\ 8H_2O$ (ZC), $A[ZrO(C_6H_6O_7)_2]\ nH_2O$ (A = Ba, Sr, Ca and Pb), $BaTiO\ (C_6H_6O_7)_2\ (C_6H_8O_7)\ 7H_2O$, $A[ZrO\ (C_4H_4O_6)_2]nH_2O$ (A = Ba, Sr, Ca and Pb), $A[TiO(C_4H_4O_6)_2\ nH_2O$ (A = Ba, Sr, Ca and Pb). The gel precursor methods such as nitrate–citrate, acetate–tartrate, acetate–amine and acetate–citrate have been developed to produce cuprate fine powders.

Spectroscopic techniques such as IR, NMR (solution and solid state) and EPR (X-band) were employed to characterize the precursors, intermediate compounds and the resultant oxides. Powder XRD, EDAX, surface area measurements (BET method), particle size analysis (sedimentation and light-scattering techniques) and microscopic techniques such as SEM and TEM were employed to characterize the samples. Physical measurements such as dielectric measurements (LCR bridge), conductivity measurements (four probe) and magnetic measurements (VSM) have also been carried out on the precursor-derived samples on appropriate processing.

3. Results and discussion

The novel metastable tetragonal phase stabilization in ZrO_2, derived from AZC, HZC and ZC, has been investigated. The precursor decomposition results in the formation of nanosized t-ZrO_2 in the temperature range 500–550°C. The metastability of citrate-derived t-ZrO_2 is attributed to a combined effect of crystallite size (9–15 nm) and lattice strain (3 to 1×10^{-3}) up to a crystallite size of about 15 nm. Above 50 nm size, the lattice strain is relieved and hence only the size effect decides the metastability. The presence of various anion vacancy configurations, predominantly the Zr^{3+}-$V_{\ddot{o}}$, has been identified from EPR studies in tetragonal as well as monoclinic (m) ZrO_2. The metastable t-ZrO_2 has been found to react with citrate-derived $BaCO_3$ to form $BaZrO_3$ at 700°C. Isothermal kinetic study has been carried out for this reaction to extract the kinetic parameters. By employing Carter model, an activation energy of 190-210 KJ mol^{-1} has been derived. The enhanced reactivity of t-ZrO_2 has been attributed to the fine particle size as well as $t \rightarrow m$ polymorphic transformation (Hedvall effect). This feature has been explored for the low temperature synthesis of zirconate perovskites.

The preparation of a new series of mixed metal citrate complexes, $M[ZrO(C_6H_6O_7)_2]nH_2O$ (M = Ba, Sr, Ca and Pb) has enabled the synthesis of respective fine-particle oxides at temperatures as low as 650°C. The genesis of perovskite phase from citrate precursors has been investigated by employing dynamic thermoanalytical techniques as well as isothermal calcination experiments. The intermediates of thermal decomposition isolated at different stages have been subjected to various physicochemical characterization techniques. Based on the experimental results a thermal decomposition scheme has been proposed. The citrate precursors decompose to produce corresponding zirconate perovskites through three major stages, *viz.*, (i) dehydration, (ii) decomposition of the citrate in a multistep process to form a mixed metal oxycarbonate intermediate, $M_2ZrO_2O_5CO_3$ (M = Ba, Sr, Ca and Pb), and (iii) decomposition of the mixed metal carbonate to form the resultant oxide $MZrO_3$. At no stage, MCO_3(M = Ba, Sr and Ca) and ZrO_2 have been identified as intermediates during the course of precursor decomposition. The supporting evidence stems from TG, isothermal calcination experiments, X-ray powder diffraction, electron diffraction and C^{13}-solid-state NMR. The resultant oxides have been found to consist of submicron particles of about 0.1 μm size with an average agglomerate size ranging from 3 to 7 μm.

The barium titanyl citrate precursor, $Ba[TiO(C_6H_6O_7)_2](C_6H_8O_7)\cdot 7H_2O$ has been found to produce fine $BaTiO_3$ powders at 600°C. Thermal decomposition of the precursor resulted in an oxycarbonate $Ba_2Ti_2O_5CO$ in the temperature range 500–550°C. The resultant $BaTiO_3$ has been found to be a mixture of cubic and tetragonal phases. Calcining the oxide above 750°C resulted in a complete tetragonal phase formation as inferred from XRD. The green densities of the $BaTiO_3$ compacts have been found to be about 60% of the theoretical value. Sintering the compact at 1300°C for 2 h resulted in a densification of about 93 to 98% with about 0.5 μm grain size. Increasing the sintering temperature to 1350°C resulted in a drastic grain growth to around 40 m. The dependence of dielectric constant upon the grain size of citrate-derived $BaTiO_3$ has been investigated and the results compared with the alkoxide-derived as well as conventionally processed samples.

Pechini gel method has been adopted for the synthesis of PTCR compositions (donor doped, donor and acceptor Co-doped $BaTiO_3$ ($La_{0.0015}$), $BaTiO_3$ ($La_{0.003}$ $Mn_{0.0001-0.001}$) Improved PTCR behaviour has been observed for the sintered compacts.

The potential chelating ability of tartaric acid has also been utilized to synthesize various mixed metal oxides. The titanyl tartrate species in aqueous solution, $TiO(H_2Tart)_2^{2-}$ with a stability of $\log \beta = 10.75$ has been found to be the key to form a series of complexes, $M[TiO(H_2Tart)_2].nH_2O$ (M = Ba, Sr, Ca and Pb). These complexes could be precipitated in aqueous conditions and isolated as fine free-flowing powders. These precursors on thermal decomposition at 650°C produce $MTiO_3$ (M = Ba, Sr, Ca and Pb) fine powders. Similarly, zirconyl tartrate complexes. $M[ZrO(H_2Tart)_2]nH_2O$ have been prepared at optimized conditions and decomposed to obtain corresponding zirconates at about 650°C. Here again, the formation of mixed metal oxy carbonate intermediates, $M_2Ti_2O_5CO_3$ and $M_2Zr_2O_5CO_3$ has been identified

Citrate gel route has been employed to synthesize $La_{2-x}M_xCuO_{4-\delta}$ (M = Ba and Sr; $0 \le x \le 0.2$). The powder characteristics and sintering behaviour have been investigated. $La_{2-x}Gd_xCuO_4$ ($0 \le x \le 2$) compositions have been synthesized at low temperature and short durations of heating (750°C–4 h). The striking feature of the citrate process is the stabilization of T^* phase in the compositional regime for $0.45 \le x \le 0.8$, $T \times T^1$ phases for $0 \le x \le 0.45$ and T^1 phase for $1 \le x \le 2.0$. The presence of only the gadolinium moment in T^* phase has been inferred from susceptibility measurements in the temperature range 30–300 K.

Carboxylate-based 'sol-gel' methods have been developed for the synthesis of fine 1-2-3 oxide powders. They include: (i) modified citrate method, (ii) homogeneous tartrate method, and (iii) regulated amine complexation process

These precursors have enabled an intimate mixing of constituent metal ions in the solution–sol–gel phases. The resultant gels have been found to decompose at 500°C to produce highly reactive, well-dispersed fine particulate mixture of $BaCO_3$, Y_2O_3 and CuO. A calculation temperature of 880–900°C has been found to produce phase pure 1-2-3 oxide fine powders. The primary particle size is of the order 0.3–1 μm and the surface area varies from 3 to 0.5 $m^2 g^{-1}$ depending on the nature of the precursor. The oxygenated powder exhibits a T_c onset at 92 K for magnetic susceptibility and a narrow hysteresis for magnetization with H_{c1} and J_c values of 105 Oe and 6×10^4 A cm^{-2}, respectively, at 77 K. The twins and defect configurations present in these powders have been examined using HREM and electron diffraction techniques. The precursor-derived oxide powders on compaction and sintering at 950°C attain the densities of 85–95% of the theoretical value. The resultant sintered discs exhibit sharp resistivity drops, $\Delta T_c = 0.5$ K with the onset of superconductivity at 92 K. The transport critical current, J_{cr}, of these compacts is of the order of 100–200 A cm^{-2}. These compacts are free from compositional deviations, second-phase inclusions and grain boundary segregations as inferred from EDAX technique.

References

1. GALLAGHER, P. K. AND THOMSON Jr. J. — *J. Am. Cer. Soc.*, 1965, **48**, 644–647.
2. GOPALAKRISHNA MURTHY, H. S., SUBBA RAO, M. AND NARAYANAN KUTTY, T. R. — *J. Inorg. Nucl. Chem.*, 1975, **37**, 891–898.

3. GOPALAKRISHNA MURTHY, H. S., SUBBA RAO, M. AND NARAYANAN KUTTY, T. R. *J. Inorg. Nucl. Chem.*, 1975, **37**, 1875–1878.

4 RAVINDRANATHAN THAMBI, K., SUBBA RAO, M., SCHWARZ, W., GRATZEL, M AND KIWI, J. *J. Chem. Soc., Faraday Trans.*, 1988, **84**, 1703–1713.

5 RAJENDRAN, M. AND SUBBA RAO, M. *Bull. Mater. Sci.*, 1991, **14**, 367–375.

Thesis Abstract (Ph.D.)

A theoretical study of the linear and nonlinear optical properties of conjugated systems by I. D. L. Albert

Research supervisor: S. Ramasesha
Department: Solid State and Structural Chemistry Unit

1. Introduction

Organic molecules with large nonlinear optical (NLO) properties have been of interest to the experimental and theoretical chemist and physicist[1]. Of the various organic systems studied it has been found, from both experiments and theory, that organic molecules with extended π-conjugation produce anamolously large second- and third-order nonlinearities. Thus the major concern of both the experimentalist and theorist is to model systems with large nonlinear optical properties We have computed NLO properties of different conjugated systems using the correlated Pariser–Parr–Pople model Hamiltonian. The results of these calculations have been used in the understanding of the reason for the exceptionally large NLO responses exhibited by these systems and to model systems with large NLO coefficients.

2. Model Hamiltonian and computational procedure

The interacting model Hamiltonian used in all our calculations in the Pariser–Parr–Pople Hamiltonian which can be written in the second quantized notation as

$$H = \sum_{i} \sum_{\sigma} \langle i|f|_i\rangle\, a^{+}_{i\sigma}\, a_{j\sigma} + \sum_{k} \sum_{\sigma\sigma'} \langle ri,gl|kk\rangle\, a'_{i\sigma}\, a^{+}_{i\sigma}\, a^{+}_{i\sigma'}\, a_{i\sigma'}$$

where $a^{+}_{i\sigma}(a_{i\sigma})$ creates (annihilates) an electron at the ith site with a spin σ. The integrals $\langle i|f|J\rangle$ represent the site energy when $i=j$ and the transfer integral or the resonance integral (β) when $i=j$. The two-electron integral in the second term represents the Coulomb interaction between electrons on the same site when $i=k$ and the intersite interaction when $i=k$ which is parametrized according to Ohno. All these integrals are parametrized to match the optical gaps of the chosen system. The Hubbard Hamiltonian is also used in understanding the effect of correlation on the NLO properties. We have always used the valence bond diagrams as the basis in all our calculations. These are chemically intuitive and a convenient way of representing configurations encountered in the configuration interaction (CI) calculation. Using the above Hamiltonian and the valence bond diagrams as the basis the Hamiltonian matrix is set up and is solved for a few low-lying eigenvalues using the Reitrup algorithm. While the finite-field method has been used to calculate the static polarizability, the recent Variational method[2] for the computation of NLO coefficients has been used to calculate the frequency-dependent polarizability and hyperpolarizability. Since we perform a complete CI calculation within the chosen model Hamiltonian our calculations are exact.

3. Results and discussion

Interaction between stacks of polyenes has been calculated within the charge dipole approximation[3]. The validity of the approximation is tested using exact calculation on small model systems The method has been applied to finite polyenes to study the shift in the group and dipole allowed excited states and hence optical

gaps in the presence of neighbours. The calculations show a red shift in the optical gaps of the infinite polyene by 0.124 eV which is rather small compared to the experimental red shift. This could be traced to the larger inaccuracy in the calculated shift in the excited state. The shift in the ground state energies is more accurate and hence the method is better suited for studying the effect of intermolecular interactions on the properties of the ground state.

The model exact energy and the polarizability calculations on unsubstituted polyenes show that the dipole allowed excited state of long-chain polyenes exhibit sudden polarization. This is a consequence of one of the single excited states becoming degenerate with the the dipole allowed excited state and implies sudden polarization in the excited singlet state as well. In the case of push–pull polyenes we find that there is a sudden increase of the dipole moments in one of the low-lying excited states at a twist angle of 90° around a double bond. This phenomenon is independent of the push–pull strength and is also insensitive to the position of the substituents[4].

Calculations of polarizability and THG coefficients of butadiene including both the σ and the π orbital vindicate the σ–π separability approximation. It is found that while the contribution of the σ electrons to the polarizability is positive and larger, the contribution of the same to the THG coefficients is small and negative. These observations lead us to infer that a pure π-electron model with electron correlations is adequate for modelling the NLO properties of conjugated systems[5]. Calculations of the SHG coefficients of substituted polyenes with more than one substituent show that the two-state model is inadequate in these systems because of the presence of more than one excited state with large transition dipole moment. The nonresonant SHG coefficients are enhanced when all the push groups are placed from one end of the polyene and all the pull groups from the other. This arrangement leads to both large difference in the dipole moments between the ground and excited states and a large transition dipole moment between these states. Finally, the twisting of the configurations around a double bond increases the SHG coefficients in all the cases provided the conjugation pathway is not blocked by such twists. Calculations on polymethineimines (PMI) and poly-(2, 3) diazabutadienes (PDB) show that the PMIs are good candidates for SHG applications. The alternating donor acceptor character along the chain leads to both large SHG coefficients and strong length dependence of these coefficients. These calculations show that the PDB systems, however, are unlikely to be efficient NLO materials[6].

Electric field-induced second harmonic (EFISH) generation coefficients of polyenes have been calculated solving for the ground state in the presence of a dc field and using this ground state wavefunction the SHG coefficients depend on the field strengths and direction. The size dependence obey a power law and have almost the same exponent and that of the THG coefficients. The coefficients are sensitive to the backbone stereochemistry and show rapid increase with the twist angel but suddenly drop to very small values at $\Theta = 90°$ when transfer across the two fragments of the polyene chain vanishes. The effect of the dc field on the SHG coefficients of substituted polyenes is almost the same as the EFISH coefficients, although the coefficients depend on the field direction relative to the push–pull direction. The size dependence is slightly weaker than the EFISH coefficients[7]. Calculations of the THG coefficients of nitrogen-containing compounds show that the symmetric cyanine dyes exhibit very large NLO response. It has been found that the presence of nitrogen at the ends of the chain aids in the polarization of the molecules and hence increases the NLO coefficients. The presence of nitrogen at the middle reduces the delocalization of the π electrons and hence reduces the NLO coefficients. Numerically exact Pockels and Kerr coefficients of both substituted and unsubstituted polyenes have been calculated by calculating the polarizability of the system in the presence of a dc field and fitting the data to a generalized parabola. We find that in the case of the unsubstituted polyenes the Pockels coefficients vanish and the Kerr's coefficient is the largest when the field is applied along the chain direction. In the case of the substituted polyenes the Pockels coefficients are very sensitive to the strength of the substituent while the Kerr coefficients are only weakly affected. A comparison of the various second-order NLO coefficients shows that the Pockels coefficients are larger than the SHG coefficients. In the case of the third-order process the trend is Kerr coefficients are larger than the the EFISH coefficients which are larger than the THG coefficients.

References

1. Chemla, D. S. and Zyss, J. *Nonlinear optical properties of organic molecules and crystals*. 1987, Academic Press.

2	SOOS, Z G AND RAMASESHA, S	*J Chem Phys*, 1989, **90**, 1067–1078.
3	ALBERT, I D L AND RAMASESHA, S	*Phys. Rev. B*, 1989, **40**, 8516–8523.
4	ALBERT, I D L AND RAMASESHA, S	*J. Phys. Chem*, 1990, **94**, 6540–6547.
5	ALBERT, I D L AND RAMASESHA, S	*Chem. Phys Lett.*, 1991, **182**, 216–219.
6	ALBERT, I. D L, RAMASESHA, S AND DAS, P K.	*Phys. Rev B*, 1991, **43**, 7013–7020.
7	RAMASESHA, S. AND ALBERT, I. D L.	*Phys. Rev B*, 1990, **42**, 8587–8599.

Thesis Abstract (M.Sc. (Engng))

Estimation of thermophysical properties of binary organic solutions–surface tensions by S. Srinivas Shastri

Research supervisors: T. R. Das and A. K. Mukherjee
Department: Chemical Engineering

1. Introduction

Surface tension is a property that represents the changes in molecular interactions and could thus be used as a means of interpreting behaviour of binary and other systems Although much work has been done in understanding this property there are only a few instances where this has been studied by considering a homologous series.

The advantage of a homologous series is the gradation of properties that can be achieved, and would enable the development of a correlation, which was the main purpose of this work, in addition to a qualitative understanding. To this end, solutions of benzene, toluene and xylene with *n*-paraffinic alcohols were studied at 25°C The chemicals used were of AR grade except xylene which was a mixture of *ortho*, *meta* and *para*. The other chemicals were not purified further

2. Experimental

The instruments used to measure the surface tension were Cahn 2000 electrobalance and stalagmometer. The principle of the Cahn balance is the tensiometric principle and the stalagmometer on the drop weight method. The instrument used to measure the density was an Anton Paar DMA 55 densitymeter.

3. Results and discussion

The study of density was necessitated for two reasons; firstly, as a means of calibration (*i.e*, mole fraction of solute) and secondly as a parameter In all cases, the density of the solution was found to be monotonically increasing with concentration of the solute (benzene, toluene or xylene). It should be stated at this point that the components (alcohols and BTX) were miscible in all proportions.

Figures 1 to 3 show the surface tension *vs* mole fraction of solute curves. It is important to note the almost linear nature of the methanol and ethanol curves and the sluggish behaviour of the curves of the other alcohols The near linearity of the methanol and ethanol curves can be attributed to the reasonably high dielectric constant which implies intermolecular hydrogen bonding[2]. With increase in BTX concentration the hydrogen-bonded complexes merely break, thus the surface tension increase is seen to be proportional to the degree of complex breakage. In the case of higher alcohols a factor that comes into play is the steric hindrance[3]. This can explain the sluggish behaviour of these curves at low concentrations of BTX.

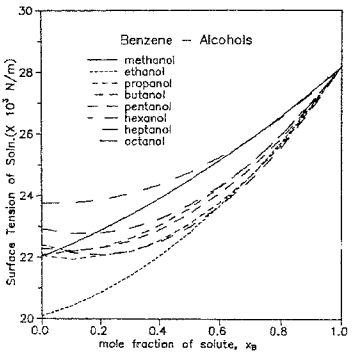

Fig 1 Surface tension *vs* mol frac.

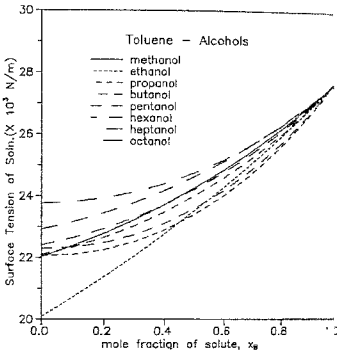

Fig 2. Surface tension *vs* mol frac

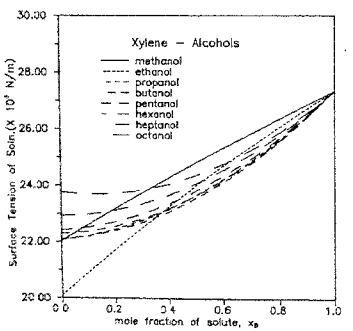

Fig 3 Surface tension *vs* mol. frac.

The major portion of this work was the development of a generalized correlation. The definition of surface tension is the surface-free energy per unit area. When a solution is formed there are energy changes which could be seen as changes in the free energy. Thus it seemed reasonable to consider the excess free energy of mixing as a parameter. The drawback with this approach is the difficulty in measurement and the next best alternative was the activity coefficient. One is aware that the activity coefficient is an adequate representation of the excess free energy and a parameter that can be either measured experimentally or obtained theoretically by means of group contribution methods such as UNIFAC[3].

The proposed correlation has the following form:

$$\frac{\sigma_{sol}}{\sigma_{alc}} = C(1.0 + A\gamma + B\gamma^2) \quad (1)$$

where σ_{alc} is the surface tension of the pure alcohol species, C, purely an alcohol number coefficient represented by

$$C = 0.88 - 0.03N, \quad (2)$$

where N is the number of $-CH_2-$ groups A and B are coefficients particular to the alcohol species and are representative of the contributions due to the dispersive forces[4], hydrogen bonding and steric hindrance. The relation for these coefficients is

$$A = 0.163 + 0.06N + 0.001N^2 \quad (3)$$

and

$$B = -[0.01 + 0.001N + 0.002N^2] \quad (4)$$

where N is the number of $-CH_2-$ groups. The activity coefficient, γ, is the activity coefficient of the alcohol species in solution, thus the relation as presented here is based only on the alcohol species, and this is the reason for reducing the surface tension with respect to the surface tension of the pure alcohol.

It is observed from the above correlation that the presence of the other component (*i.e.*, BTX) is not important. This implies that the coefficients are fairly insensitive to the presence of the other component. However, the effect of the other component comes into play in the activity coefficient.

This correlation is quite accurate showing a maximum absolute deviation from experimental that in no case exceed 5%. The limitation of this correlation is that it is specific to 25°C and end point calculation of the surface tension is not possible.

4. Conclusions

1. Group interactions definitely play a role in the behaviour of surface tension.
2. The activity coefficient and the excess free energy are good representations of the changes in surface tension.
3. It is observed that dispersive forces which are generally quite significant in mixtures of non-electrolytes are also very important in the mixtures studied in this work.
4. The activity coefficient of the alcohol species has been found to be a good parameter to base the correlation.
5. The correlation developed is generalized and the coefficients A, B and C are characteristic of the alcohol component only and are fairly insensitive to the other component

References

1. Shastri, S. S., Das, T. R. and Mukherjee, A. K. — The effect of group contribution on the surface tension. *Indian Chemical Congress*, Madras, Dec. 18–21, 1991.
2. Pimental, G. C. and McClellan, A. L. — In *The hydrogen bond*, pp. 1–66, 1960, W. H. Freeman
3. Fredenslund, A., Jones, R. L. and Prausnitz, M. J. — Group contribution estimation of activity coefficients in nonideal liquid mixtures, *AIChE J.*, 1975, **21**, 116–128.
4. Shinoda, K. — Iceberg formation and solubility, *J. Phy. Chem.*, 1977, **81**, 1300–1302.

Thesis Abstract (Ph.D.)

Theoretical studies of electronic effects in organic molecules and reactive intermediates by S. Lalitha

Research supervisor: J. Chandrasekhar
Department: Organic Chemistry

1. Introduction

The work involves the quantification of different types of orbital interactions that operate in a variety of organic systems and the elucidation of their consequences on molecular and electronic structures, energetics, as well as on reactivity.

A variety of experimental procedures are commonly used to determine and quantify electronic effects. Theoretical methods are also quite powerful for the study of such problems. Several procedures including molecular mechanics, semiempirical (MNDO) and *ab initio* MO methods have been used in the present investigation.

1

2

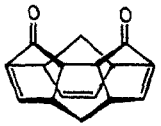

3

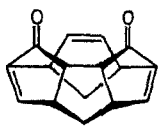

4

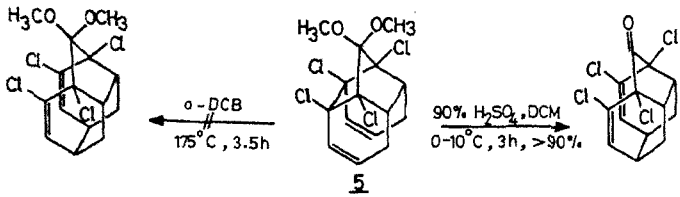

5

SCHEME 1. (contd)

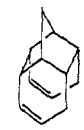

6

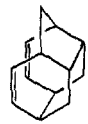

7

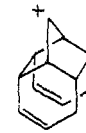

8

9

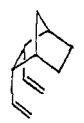

10

11

12

13

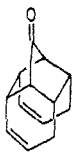

14

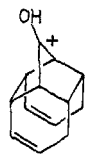

15

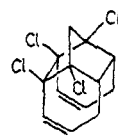

16

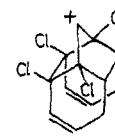

17

SCHEME 1.

2. Ground states of diradical systems

The role of various interactions in influencing the preferred electronic structures of diradicals is studied. The determination of the ground states of diradical species and *reliable* prediction of the associated singlet–triplet energy separation has been a controversial problem in both experimental and theoretical chemistry. The main computational difficulty is that different procedures are often used for studying the singlet and triplet states. A procedure to circumvent this problem by using the UHF methodology uniformly is suggested. Using a semiempirical correlation, numerous predictions are made for the preferred ground estates as well as the S–T energy gaps of a number of diradical systems. The systems examined include species such as twisted π systems, (1, 3) and (1, 4) diradicals, non-Kekule hydrocarbons like trimethylenemethane, tetramethy-

leneethane, polycyclobutadiene, benzynes, pyridnes, etc. Calculations carried out at the MNDO level, with full geometry optimizations for all the diradicals, lead to results in excellent agreement with available *ab imtio* as well as experimental studies. The only discrepancy, that of the predicted preference of tetramethyleneethane for the singlet ground state, is resolved by proposing a plausible reinterpretation of the experimental results[1]. The calculated results are rationalized on the basis of the interplay between through-space (overlap and spin-pairing) effects and through-bond spin polarization effects.

3. Alpha and beta silyl effect on vinyl radicals

The geometric, conformational, and energetic consequences of α- and β-silyl groups at vinyl radicals are evaluated using the *ab initio* theory. Calculations at the 6-31G*/ /STO-3G* level reveal that the α-silyl effect is quite substantial and larger than that of the corresponding α-methyl effect. In contrast, the β-silyl group produces little perturbation in the structure and energetics of vinyl radicals.

4. Homoaromaticity in organic molecules and reactive intermediates

The magnitude of homoaromaticity is evaluated in numerous organic systems using the MNDO methodology including limited configuration interaction. A variety of criteria such as thermodynamic stabilization relative to nonstabilized reference systems, atom–atom energy partitioning, bond orders, geometric distortions and UHF instabilities have been applied. The principal conclusion is that homoaromaticity is not important in neutral and anionic systems. However, some of the cationic systems do show substantial homoaromaticity. A tricyclic model system is proposed to distinguish between alternative stabilizing interactions in carbanions. MNDO calculations are used to demonstrate that the contributions from tris-homoconjugation, inductive effect, and negative hyperconjugation can all be swamped by gegen-ion interactions.

5. Structural and electronic effects in roofed polyquinanes

The structural and electronic effects in roofed polyquinanes, **1–4**, which provide a possible route to the synthesis of dodecahedrane, are investigated. Molecular mechanics calculations indicate that the *trans* double bonds in these systems are hyperstable and hence should resist hydrogenation[2]. However, the magnitude of hyperstability is controlled by remote steric interactions in the cage molecules. The double bonds in these molecules have interesting electronic interactions as well. MO calculations and an empirical analysis are used to assign the photoelectron spectra of these and related model compounds. The symmetric and antisymmetric combinations of the πMOs of the enone moieties and **3** and **4** show some of the largest splittings ever measured[3]. The results indicate that through-space and through-bond effects act in concert in these systems, as in propano-bridged systems.

6. Cope rearrangement catalysed by a remote carbenium ion centre

The electronic origin of a remarkable acceleration of the Cope rearrangement in a tetracyclic molecule (**5**) effected by a remote carbenium ion centre (Scheme 1) is unravelled using MNDO calculations[4]. Detailed reaction energy profiles were computed at the MNDO level for the model system **6**→**7** and **8**→**9**.

The computed results throw new light on the mechanistic possibilities of Cope rearrangements and contribute to a general understanding of remote substituent effects on such reactions. Calculations on model systems **10–13** indicate that the presence of norbornyl skeleton and the rigid endocyclic double bonds affect the mechanism and energetics of Cope rearrangement to a considerable extent. The effect of substitution at the 7-position of the norbornyl skeleton and the effect of chlorine substitution as in the original system **5** have also been examined by taking the model systems **14–17**.

References

1. CHAKRABARTY, A., ALBERT, I. D. L., RAMASESHA, S., LALITHA, S. AND CHANDRASEKHAR, J. Is tetramethyleneethane a ground state triplet?, *Proc. Indian Acad. Sci. (Chem. Sci.)*, 1993, **105**, 53–62.

2. LALITHA, S., CHANDRASEKHAR, J. AND MEHTA, G. Cage geometry controlled hyper stability in roofed polyquinanes, *Tetrahedron Lett.*, 1990, **31**, 4219–4222.

3. *LALITHA*, S., *CHANDRASEKHAR*, J. AND MEHTA, G. *Remarkable acceleration of Cope rearrangement by a remote* carbenium ion center. Theoretical elucidation of the electronic origin, *J. Org. Chem.*, 1990, **55**, 3455–3457.

4. MEHTA, G., REDDY, K. R., GLEITER, R., LALITHA, S. AND CHANDRASEKHAR, J. Roofed polyquinanes: Synthesis and electronic structure, *J. Org. Chem.*, 1991, **56**, 7046–7055.

Thesis Abstract (M. Sc. (Engng))

A design-evaluation system using medical axis transforms by V. Sundararajan

Research supervisor: B. Gurumoorthy
Department: Mechanical Engineering

1. Introduction

The traditional product development cycle from conceptual design to the realization of the product goes through several iterative procedures. The traditional cycle begins from the process of conceptual design and proceeds through the tasks of detailed design and drafting, design analysis, prototype building and testing and ends with the realization of the part. After each stage in this cycle, if the results are not satisfactory, the part has to be redesigned in order that it finally performs satisfactorily in the working environment. There is, therefore, a large time gap between the concept and the final realization of the part due to these iterative procedures.

Automation of these procedures will reduce the lead time. Although design and manufacturing activities are individually automated to a large degree, the transition from design to manufacturing is still a problem where large time gaps exist resulting in a bottleneck. This is because each stage/activity needs geometric information at different levels of detail and abstraction (These geometric entities which form domain-dependent regions of interest are termed as 'features').

In general the design system has information about where the material is while the machining task requires geometric details of the material to be removed from the billet to get the final form of the part. Presently the interpretation of geometric information is done by human operators, resulting in time delays and inefficiencies.

2. Design evaluation systems

One solution to this problem is to automatically extract the required geometric information from the available representation in each module/activity. Algorithms for feature extraction in general use an *intermediate* representation which makes the task of extraction and further manipulation easy. The transformation to obtain this intermediate representation must be isomorphic so that the transfer of information between the two representations is easy. Any modification in the intermediate representation can therefore be realized in the object representation. Medial axis transform[1,2] has been proposed as one such intermediate representation for feature extraction and reasoning.

Here, we have attempted to build a system that closes the loop between design and manufacturing using the MAT. The output of the design-evaluation system will be a design that is manufacturable.

3. Medial axis transform (MAT) of an object

MAT is defined as the locus of the centres of maximal disks (2D)/spheres (2D) that can be placed within an object such that these disks/spheres are tangential to at least two edges/faces and that these disks/spheres do not cut any third edge/face of the object[1].

The advantages of the MAT are:

- Connectedness: One can traverse along from one point to any other point on the MAT. There are no discontinuities.
- Unique representation: From an MAT only one object can be derived, conversely an object will derive only one MAT.
- Reduction of dimension: MAT reduces the dimensionality of the object by one. This is good because manipulation at a lower dimension will be easier than at higher dimension.

4. Implementation

Features are extracted from the MAT and manufacturing tagged on to these features. These features can be evaluated by an expert system. The criterion of evaluation is the manufacturability of the object. Once the evaluation is performed, remedies suggested by the expert are incorporated into the MAT and finally the model of the manufacturable part is obtained from the modified MAT.

An algorithm to generate the MAT of 2.5D objects with rectilinear edges has been explained. The proposed methodology is an improvement over those reported in literature[3-5] in that only the end points of the MAT segments are determined to generate the MAT. Curvilinear edges in objects are handled by splitting them into rectilinear segments.

Heuristics for feature extraction from the information available from the MAT has been outlined. This information is input to an evaluation module. Presently it is assumed that an expert system which contains rules of the specific manufacturing process exists. The outputs of the evaluation system are modifications to be performed on the object. These modifications are incorporated into the MAT and a modified MAT of an object that is manufacturable is obtained.

Finally, an algorithm to regenerate the B-rep model of the object from the modified MAT has been suggested and implemented. The rules to regenerate the object depend on tangency information as the MAT has information of the circles at the ends of each segment.

5. Results and conclusions

While the use of MAT as an intermediate representation has been proposed earlier[6], this is the first attempt to close the loop between the design and manufacturing using MAT as an intermediate representation. Algorithms have been proposed and implemented to:

- generate MAT from a B-rep model
- use MAT for feature extraction and modification
- regenerate the B-rep of an object from its MAT.

A design evaluation system has been built, using these algorithms, to evaluate and modify a given part model to realize a part that is manufacturable. The system has been tested using models of parts to be stamped (2.5D multiply connected polyhedral objects).

It is found that the shape of the MAT is sensitive to the dimensions of the object. During modification of the MAT to incorporate the expert's suggestions, it is necessary to predict the change in the shape of MAT as the object geometry changes. In this work, heuristics have been used to predict the change in shape of the MAT due to suggested modifications in the object geometry for 2.5D polyhedral objects. This task however will be very tedious as the complexity of the objects and the feature domain increases. Extension of the use of MAT for more complex domains and 3D objects may therefore not be very straightforward and requires further investigation.

References

1. Blum, H. and Nagel, R. N. *Pattern Recognition*, 1978, **10**, 167–180.
2. Nackman, D. R. and Pizer, S. M. *IEEE Trans.*, 1985, **PAMI-7**, 187–202.
3. De Souza, P. V. and Houghton, P. *Comput. Biomed. Res.*, 1977, **10**, 333–343.

4 LEE, D. T. *IEEE Trans.*, 1982, **PAMI-4**, 363–369.

5. XIA, Y. *IEEE Trans.*, 1989, **PAMI-11**, 1076–1086.

6. HALL, M. A., SUDHALKAR, A. M., GADH, G., GURSOZ, E. L. AND PRINZ, F. B. Presented at the *Winter Annual Meeting of ASME*, November 25–30, 1990.

These Abstract (Ph.D.)

Some studies on negative resistance behaviour associated with MOSFET by C. Guru Prasad

Research supervisors: M. Satyam and D. B. Ghare
Department: Electrical Communication Engineering

1. Introduction

The integrated circuit (IC) is an important component of the electronic systems that we use today. The invention of integrated circuit, where a large number of devices are fabricated on a small portion of the wafer, has led to the development of fast, reliable and economical systems[1]. The continuous effort to miniaturize has resulted in developing ICs with component densities of the order of 10^5–10^6 per cm^2. At these levels of miniaturization, physical and technological problems are encountered which limit further reduction in device dimensions[2]. One such factor is the appearance of negative resistance in the *V–I* characteristic of a device due to high electric field or due to the interaction of parasitic components associated with the device. The negative resistance behaviour can lead to instabilities if the device is operated in this region. However, it is also possible to increase the range of application of these device structures by utilizing the negative resistance behaviour. Though there had been many investigations on the drain-source breakdown phenomena in MOSFETs, a thorough investigation into the occurrence of this negative resistance region and its dependence on various bias conditions is lacking[3–5]. Especially the influence of protection diode structure on this negative resistance behaviour remains to be investigated. In view of this, an attempt has been made in this thesis to investigate the negative resistance characteristics that arise in a device, namely, MOSFET, at high electric fields as well as due to its interaction with the parasitic devices.

2. Experimental work

The *V–I* characteristics of an *n*-channel MOSFET in a typical CMOS IC, such as CD4007, have been measured up to drain voltages of the order of 35 V (which is two to three times the normal operating voltage) under different gate and substrate bias conditions and temperatures. The effect of substrate voltage under various operating conditions of MOSFET, such as gate voltage less than threshold, near threshold and much greater than threshold, has been investigated. These experiments have been carried out at low temperature (77 K) also. The experimental set-up consists of a HP6623A programmable power supply, Keithly model 181 nanovoltmeter and Fluke 8842A digital multimeter, all of which have been interfaced with the PC/AT.

3. Results and discussion

It has been found from these investigations that these characteristics exhibit negative resistance regions (Fig. 1). The origin of these negative resistance regions has been identified and appropriate analysis of the processes involved has been carried out. It has been shown that the negative resistance observed at low drain currents is due to the avalanche multiplication at the drain–substrate junction which triggers the parasitic bipolar transistor, formed by source (n^+), substrate (p) and drain (n^+), into action. The occurrence of a second negative resistance at relatively high drain currents has been attributed to the conductivity modulation of the substrate because of the carriers injected at the drain end[6]. The occurrence and the extent of these negative resistance regions and the hysterisis characteristics are affected by gate and substrate voltages. Also

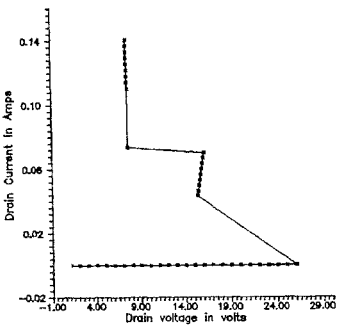

Fig. 1. Typical measured drain characteristics (n-channel FET) at VG = 0 V, V_{sub} = 0, R_{sub} = 0 Ω.

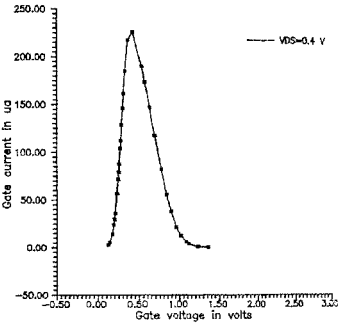

Fig. 2. Typical negative resistance characteristic obtained with RSR = 4.7 k, R_{sub} = 1 k, RDR = 100 Ω, VSR = −1.55 V.

experiments conducted at 77 K indicate that operating the device at 77 K gives better performance due to the absence of second negative resistance and bipolar transistor behaviour at low drain currents, under high substrate and gate voltages. Thus these investigations point out the limitations that arise due to the parasitics which become important at high levels of miniaturization.

After realizing that the parasitics play an important role in deciding the behaviour of ICs, a systematic study has been made of a MOSFET structure in a CMOS IC with various possible interconnections. These studies have indicated that these parasitics can be utilized to increase the functional capabilities of the integrated circuit structures.

It has been possible to realize negative resistance characteristics by providing simple interconnections between the various electrodes which are essentially the terminals of parasitic elements and the regular FET. The following are the various types of negative resistance structures that have been realized.

(i) Negative resistance in the gate voltage–gate current characteristic; the interconnection among various terminals is as follows. Drain and substrate are shorted and connected to a constant current source. Source-substrate junction is forward biased.

(ii) Negative resistance in the gate voltage–gate current characteristic has also been observed through a different configuration. Here, the source–substrate junction is forward biased. Also an external series resistor is connected along the source path. Drain–substrate junction is reverse biased and kept constant (Fig. 2).

(iii) Negative resistance in the source voltage–source current characteristic; here the device is biased in a similar manner as in the above case, but with the external series resistor connected to the gate circuit instead of the source.

These negative resistance characteristics have been explained in terms of the interaction between various parasitic elements along with the regular FET.

The utility of the negative resistance characteristics has been demonstrated by constructing a Schmitt trigger and relaxation oscillator. Thus it may be seen from these investigations that a single MOSFET structure available in an integrated circuit can be made use of to generate a variety of negative resistance characteristics which are essentially the characteristics of devices performing functions like switching, oscillation, memory, etc.[1].

References

1. GLASSER, A. B. AND SHARPHE, G. E. S. — *Integrated circuit engineering*, 1979, Addison–Wesley.
2. SABRIS, A. G. — *VLSI reliability*, Vol. 22, VLSI Electronics, Microstructure Science, 1990, Academic Press.
3. HSU, F. C., MULLER, R. S. AND HU, C. — A simplified model of short channel MOSFET characteristics in the breakdown mode, *IEEE Trans.*, 1983, **ED-30**, 571–576.
4. KOTANI, N. AND KANAZU, S. — The effect of holes on the injection induced breakdown in *n*-channel MOSFETs, *IEEE Trans.*, 1985, **ED-32**, 722–725.
5. FENG, W. S., CHAN, T. Y. AND HU, C. — MOSFET drain breakdown voltage, *IEEE*, 1986, **EDL-7**, 449–450.
6. SZE, S. M. — *Physics of semiconductor devices*, 1986, Wiley-Eastern.
7. REICH, H. J. — *Functional circuits and oscillators*, 1961, Van Norstrand.

Thesis Abstract (Ph.D.)

Analysis of laminates *without* and with delaminations at free edges by H. K. Harikumar

Research supervisors: A. V. Krishna Murthy and K. Vijayakumar
Department: Aerospace Engineering

1. Introduction

With the growing tendency to utilize layered composite materials for critical applications, a new need to understand the behaviour of damages in controlling strength of laminates has arisen. The influence of various components of damages or pattern of cracks on the strength and stiffness of the laminate differ. The damage can be grossly classified into two categories, namely, intraply and interply damage. The intraply damages consist of fibre breaks, matrix cracks, fibre disbonds, etc., which occur within a ply. Loss of adhesion between plies is an interply damage commonly known as delamination. The main attempt in this thesis has been to develop simple and yet effective theoretical models for the study of delaminations in laminates.

2. Free edge effect

Interlaminar stresses in symmetric composite laminates under inplane loading with and without delamination cracks have received wide attention since 1967[1–3]. Both experimental studies and analytical solutions have indicated that complex stress states with rapid change of gradients occur along edges of composite laminates. The occurrence of interlaminar stresses is considered to result from the presence and interactions of geometric discontinuities of the composite laminate and material discontinuities through the laminate thickness. These stresses have been found to occur only within a very local region near the geometric boundaries of the laminate, and is often referred to as a 'free edge effect'. A fundamental understanding of the interlaminar stress field associated with a free edge in laminated composites is critical in order to assure structural integrity, particularly, to develop models for delamination prediction which forms a criterion in assessing the design of structural components.

A displacement-based laminate theory is developed to determine the interlaminar stresses in symmetric laminates subjected to inplane loads. The zero shear strain conditions along the top and bottom surfaces of the laminate are satisfied a priori in the expansion for displacements in terms of the thickness-wise coordinate. Using the principle of virtual displacements, governing differential equations and boundary conditions are established. The first-order approximation of the present theory termed as 'first-order thickness-stretch deformation theory' retains the assumptions of zero transverse shear strains (through the thickness of the laminate) of the classical laminated plate theory (CLPT) (eqn 1).

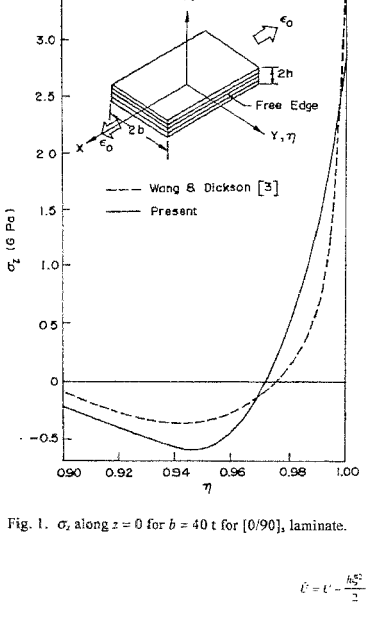

Fig. 1. σ_z along $z = 0$ for $b = 40$ t for [0/90]$_s$ laminate.

$$\hat{U} = U - \frac{h\xi^2}{2} W_1$$

$$\hat{V} = V - \frac{h\xi^2}{2} W_1$$

$$\hat{W} = \xi W. \tag{1}$$

To study its performance the model is applied to the free edge problem. The inclusion of the thickness–stretch deformation provides the necessary flexibility (over CLPT) to obtain finite statically equivalent estimates for interlaminar stresses even in the free edge problem. The results of interlaminar stresses are compared with the results obtained from a model involving layerwise series approximation of the displacement function to over 30 terms per layer[3] (Fig. 1). Reasonably good agreement is noticed. Dependence of the nature of interlaminar stresses on the ply thickness and stacking sequence is also studied.

3. Delaminations at straight free edges

As a next step, the theory is extended to include flexure and is used to obtain interlaminar stresses and strain energy release rates in a laminated coupon containing edge delaminations. The laminate is divided into various zones based on size and location of delaminations. Displacements in each region are represented according to the present theory and the required continuity and boundary conditions are satisfied. Strain energy release rate is obtained as the derivative of the total strain energy of the laminate with respect to the delamination size. The analysis also includes initial thermal strains developed during curing when the laminate is cooled down

from matrix gel temperature. In view of the displacement-based laminate plate theories used in the analysis the procedure does not mimic the stress singularity at the delamination tip. However, the magnitude of stress obtained from the present analysis brings out its severity. The case of an infinitely long symmetric laminate with delaminations located at the laminate midplane along its free edges is considered for numerical study. The results for interlaminar normal stress ahead of the delamination tip are reported for various delamination sizes. It is observed that interlaminar normal stress is more severe at the free edge of the undelaminated laminate than at the tip of the delamination of finite size. Beyond a particular size of delamination, hardly any change in the peak value of the delamination tip stress is noticed. With increasing delamination size, energy release rate rises steeply and converges to a value predicted by classical laminated plate theory[4]. This behaviour is also noticed in other results reported in the literature. The free edge delamination grows initially in an unstable manner till a particular critical size, beyond which the growth is stable.

4. Delaminations along curved edges

A methodology to estimate total strain energy release rate and its components along curved delamination fronts based on classical laminate plate theory is also presented. The present approach consists of analysing only the neighbourhood of a short segment of the delamination edge. This procedure can be readily extended to other theories including those developed in earlier chapters. In the case of delaminations along infinitely long straight edges the present methodology yields closed-form solutions for total strain energy release rate and its components. The present results for the components of strain energy release rates are compared for various stacking sequences and delamination locations with those obtained from refined quasi-three-dimensional analyses for the case of a chosen delamination length six times the ply thickness. Results show that the estimates of antiplane shearing/tearing mode G_{III} from classical laminated plate theory agree very well with those obtained from quasi-three-dimentional analysis (Fig. 2). Reasonably good agreement in other modes is also observed. For a more general application, finite element method needs to be used. Hence, finite elements based on classical laminate plate theory are used to study symmetric laminates with cutouts subjected to inplane loading containing delaminations. Comparison of the results of strain energy release rates for the case of $[0/90]_s$ by a full 3D finite element analysis confirms the usefulness of the present methodology in bringing out the qualitative behaviour of these laminates.

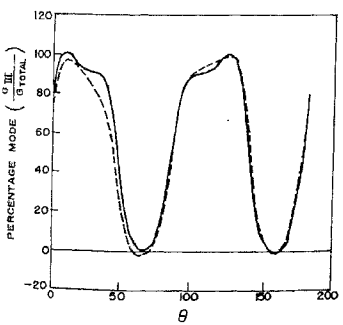

Fig. 2. G_{III} of delaminations in $-\theta/(45-\theta)$ interface of $[-(45+\theta)/-\theta/(45-\theta)/(90-\theta)]_s$ laminates; ---- Quasi 3D finite element analysis; —— Present methodology using CLPT results (in closed form).

5. Concluding remarks

Thus the main attempt in this thesis has been to develop simple theoretical methods for the study of interlaminar stresses and strain energy release rates in laminates without and with delaminations. Two-

dimensional theories are necessary to bring out, at least qualitatively, the effect of damages so that such analysis could be useful to choose more damage tolerant options at design stage and/or identify critical regions for more detailed study by three-dimensional finite element analysis. Currently such approaches called the global–local analysis are becoming attractive. The present study is a contribution towards global analysis in such a strategy.

References

1. HAYASHI, T. — Analytical study of interlaminar shear stresses in a laminated composite plate, *Trans. Jap. Soc. Aeronaut. Space Sci.*, 1967, **10**, 43–48.
2. PIPES, R. B. AND PAGANO, N. J. — Interlaminar stresses in composite laminates under uniform axial extension, *J. Composite Mater.*, 1970, **15**, 538–548.
3. WANG, J. T. S. AND DICKSON, J. N. — Interlaminar stresses in symmetric composite laminates. *J. Composite Mater.*, 1978, **12**, 390–402.
4. O'BRIEN, T. K. — Characterization of delamination onset and growth in composite laminates, *Damage in Composite Materials, ASTM STP 775*, pp. 140–147. 1982.

Thesis Abstract (Ph.D.)

Current-limiting and voltage-limiting properties of ceramics based on n-$BaTiO_3$ solid solutions by V. Ravi

Research supervisor: T. R. N. Kutty
Department: Materials Research Centre

1. Introduction

Current-limiting (CL) characteristics of donor-doped polycrystalline ceramics on $BaTiO_3$ or its solid solutions find wide-ranging applications such as self-regulating heaters, overload protection devices, degaussing components and time delay switches. Notwithstanding its wide applications, CL has received less attention in open literature, possibly due to its proprietory nature. The existing publications[1, 2] project the CL as a mere consequence of the well-known PTCR (positive temperature coefficient in resistivity) effect. The present work has been undertaken to understand the mechanism underlying the CL property. During the course of this study, we observed that the CL behaviour gives way to voltage-limiting (varistor) (VL) at specific chemical composition of the solid solution, ambient temperature, T_a, and field strength. Hence, the studies have been extended to the varistors based on n-$BaTiO_3$ ceramics.

2. Experimental procedures

The perovskite, $BaTiO_3$, and its solid solutions have been prepared by either ceramic or chemical methods (including hydrothermal method). Donor and acceptor impurities are introduced through solution mounting as well in the precursor itself. The methods employed for characterization are such as X-ray powder diffraction, thermal analysis, spectroscopic (electron paramagnetic resonance (EPR), infrared (IR)) and electron microscopic techniques. The steps involved in the fabrication and processing of ceramics including sintering schedule are studied. Electroless nickel coating has been applied to these sintered disks for ohmic contacts to measure electrical properties, *e.g.*, resistivity, capacitance *versus* temperature and current–voltage relations.

3. Results and discussion

The current (I)–Voltage (V) relations of n-$BaTiO_3$ ceramics (when $T_a < T_C$) have four distinct regions[3] (Fig. 1a) in the increasing order of applied potentials; (i) a linear portion at lower voltages which includes a current

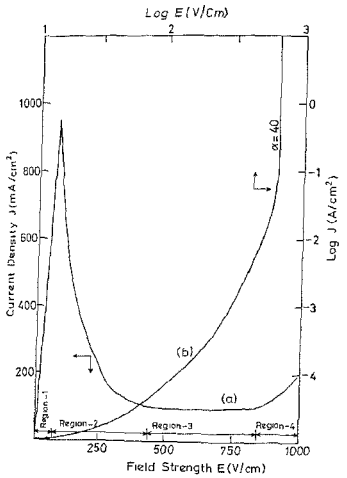

Fig. 1. J–E characteristics of (a) $BaTiO_3$: 0.3 La, and (b) $(Sr_{0.4}Ba_{0.6})(Ti_{0.97}Zr_{0.03})O_3$: 0.3 La at 300 K.

maximum (J_{max}), (ii) a negative differential conductivity (NDC) region, (iii) a nearly constant current segment (J_{nn}), and (iv) a slow upturn behaviour. For the bulk compositions having isovalent lattice substituents, the NDC region is broadened out and the attained body temperatures (T_b) at the CL regions vary with the composition. The measured T_b values in the NDC as well as the CL region depend upon T_a. The T_bs attained during CL are much lower than Curie temperatures (T_C). The dissipation characteristics show that the power-handling capability of these ceramics decreases drastically when $T_a > T_C$. The I–V curves also change from CL to VL behavior, when T_b and T_a are always $> T_C$. These changes are observed in the titanate solid solutions (Fig. 1b) as well, so that the varistor behaviour could be brought to room temperature by modifying the bulk composition. The present observations show that CL arises out of the combined influence of the field effect, Joule heating and heat dissipation rather than as a mere consequence of the PTCR property. Joule heating raises the cubic phase content much below T_C as a consequence of the diffuse phase transformation behaviour of n-$BaTiO_3$ solid solutions. X-ray powder diffractograms recorded during CL show the presence of cubic phase, the content of which increases depending upon the magnitude of applied potential as well as T_a. Whereas the heat dissipation to the surrounding forces the grains to fall back to the tetragonal phase, when $T_a < T_C$. The charge trapping behaviour of the midband-gap states, particularly of the acceptor type, is different in the tetragonal as compared to that of cubic phase. This imparts a heterojunction character to the tetragonal/cubic interface regions. Hence, tunneling across such asymmetric barrier, generated, under Joule heating, will account for the CL characteristics which show good comparison to the reported I–V curves of metal–insulator–semiconductor heterojunctions. The calculated I–V relations are in good agreement with the experimental curves. In Region 4, because of higher T_b attained, the heat dissipation is inadequate for phase reversion tetragonal, accounting for the upturn behaviour.

The influence of ATS mixture ($Al_2O_3 + TiO_2 + SiO_2$) on the I–V characteristics of n-$BaTiO_3$ is examined in detail. Two novel wet chemical techniques consisting of two-stage firing have been developed to incorporate these additives to eliminate the possible contamination from the grinding and mixing media utilized in the ceramic method. These techniques are particularly suited for GBL modifiers in low concentrations (< 1%). The optimum ratio among the additives (Al_2O_3 : TiO_2 : SiO_2) is found to be 1:1:3 for all the ceramic compositions. At lower concentrations, ATS decreases the room temperature resistivity (ρ_{300}) without modifying the sharp ρ–T curves, whereas at higher contents, it enhances ρ_{300} and broadens the ρ–T curves. Incorporation of TiO_2 (< 5%) does not change the electrical resistivity significantly. Al^{3+}, when doped alone, raises the ρ_{300} of n-$BaTiO_3$ to very high values. However, ρ_{300} does not increase with the addition of Al_2O_3 in the presence of SiO_2, but is quite useful as a grain size controlling additive. SiO_2 added in n-$BaTiO_3$ ceramics generates the titanosilicate phases. The latter helps to retain liquid phase up to 1520 K on cooling from the sintering temperatures. This alters the grain boundary reactions within the ceramics, which in turn, modifies the electrical properties. The broad PTCR curves observed at higher contents of ATS indicate enhanced disorder at the grain boundary layers (GBL). The disorder at the GBL regions is found to arise dominantly from the addition of SiO_2. In these ceramics, the acceptor states have a distribution in energy values. Consequently, the activation of the acceptor states located in the GBL regions persist to temperatures > T_C. Accordingly, the PTCR region is broadened. The diminished J_{max} as well as the NDC region at higher contents of ATS can be explained in terms of the concepts of field effect at the asymmetric barrier. Under these conditions, the heterojunction character at the grain boundaries is built up at lower field strengths thereby limiting the J_{max} and broadens the NDC region. The tunneling across the asymmetric barrier so generated under Joule heating accounts for the appearance of J_{lim} without the pronounced current maximum.

In the case of mixed-phase ceramics[5] prepared from sintering mixtures of donor-doped $BaTiO_3$ (tetragonal) as the major phase and undoped cubic perovskite such as $SrTiO_3$, $BaSnO_3$, $BaZrO_3$ and $BaTiO_3$ (< 20%, prepared through hydrothermal method) as the minor phase, the initial linear I–V relation (Region 1) becomes CL (Region 3) without any current maximum (Region 2). X-ray powder patterns of sintered samples show the presence of both cubic and tetragonal phases at room temperature. The resistivity continues to increase not only across the Curie point (T_C) but also at higher temperatures, without any apparent maximum even above 500 K. Thus, the PTCR region is broadened and the ratio of resistivities across T_C has decreased. The EPR (electron paramagentic resonance) spectra of $V_{Ba}^{\cdot}$ and Mn^{2+} indicate the contribution of the disorder component induced by the minor phases. The broadening of the ρ–T and the absence of NDC region in I–V curves can be explained on the same lines as that caused by ATS mixture.

The VL characteristics of n-$BaTiO_3$-based solid solutions[6] observed at room temperature have also been investigated. For example, the solid solution, $(Sr_{0.4}Ba_{0.6})$ $(Ti_{0.97}Zr_{0.03})O_3$: 0.3 La exhibits the VL action at T_a = 300 K (Fig. 1b), whereas at T_a = 260 K, CL behaviour is noticed. The leakage current, the breakdown voltage as well as the nonlinearity coefficient (α = 30–50) could be varied with the isovalent lattice substituents, the GBL modifiers as well as through post-sintering annealing. Their exceptional stability at larger field strengths and high energy-receiving capability arise from the abnormally high effective dielectric constant. Since T_a is always > T_C, the heat dissipation to the surroundings does not lead to any phase conversions. Furthermore, the acceptor states on either side of the GBL are occupied, leading to a symmetrical energy barrier with considerable width. At higher field strengths this barrier can be squeezed, and the field ionization of the acceptor states leads to tunneling through the symmetric barrier, resulting in large currents. However, within the pre-breakdown regions, the continuously changing slope corresponds to space charge limited conduction (SCLC) mechanism with the exponential distribution of trap levels. The GBL diffusion of Pb into these ceramics leads to the appearance of the CL regions at lower field strengths giving way to VL characteristics at higher field strengths. This is due to: (i) increase in T_C due to Pb incorporation, and (ii) the differential distribution of Pb between the interior and the exterior of the same grain leading to spatial differentials in T_C. As a result, the asymmetric nature of the energy barrier extends to higher temperatures. Hence, the CL extends to higher field strengths. With further enhancement in potential, the whole grain is in the cubic form under Joule heating and thus the potential barriers become symmetric, tunneling through which accounts for the varistor action.

References

1. SABURI, O. AND WAKINO, K. *IEEE Trans.*, 1963, **CP-10**, 53–67.
2. TING, Y. *IEEE Trans.*, 1972, **IA-8**, 338–344.
3. KUTTY, T. R. N. AND RAVI, V. Current-limiting property of n-$BaTiO_3$, *Mater. Sci. Engng B, Solid St. Mater Adv. Technol.*, 1994, **25**, 119–131.
4. RAVI, V. AND KUTTY, T. R. N. A novel method for the uniform incorporation of grain boundary layer modifiers to PTCR $BaTiO_3$, *J. Am. Cer. Soc.*, 1992, **75**, 203–205.
5. RAVI, V. AND KUTTY, T. R. N. Current-limiting action of mixed-phase $BaTiO_3$ ceramic semiconductors, *J. Appl. Phys.*, 1990, **68**, 4891–4893.
6. KUTTY, T. R. N. AND RAVI, V. Varistor property of *n*-$BaTiO_3$-based current-limiters, *Appl. Phys. Lett.*, 1991, **159**, 2691–2693.

Thesis Abstract (M. Sc. (Engng))

Phase transformation introduced by mechanical and chemical surface preparations of tetragonal zirconia polycrystals by Nibedita Mitra

Research supervisors: S. K. Biswas and B. N. Pramila Bai
Department: Mechanical Engineering

1. Introduction

Zirconia (ZrO_2) is a remarkable ceramic material which exhibits polymorphism. Three crystallographic modifications exist; cubic (C), tetragonal (T) and monoclinic (M). They are stable at high, intermediate, and low temperature ranges, respectively. The high toughness exhibited by ZrO_2 as it undergoes phase transformation from the tetragonal to the monoclinic under mechanical and thermal stresses is well known. In the family of engineering zirconia-based ceramics, tetragonal zirconia polycrystals (TZP) show the highest toughness.

The present work consists of structural studies of phase transformation brought about by (a) a mild cutting process, (b) subsequent etching of the cut surface, and (c) abrasion of these surfaces.

2. Experimental set-up

Rods of 3 mole % yttria-doped tetragonal zirconia polycrystals (3Y-TZP) were cut by a low-speed diamond saw using an oil lubricant. Etching was done by immersing 3Y-TZP surface in boiling orthophosphoric acid (H_3PO_4) solution for different times at a temperature of 170°C. The structural change induced by cutting and etching was compared with other mechanically/chemically treated surfaces. Further, the cut surface and the cut and etched surface were rubbed against silicon carbide (SiC) abrasive cloth (400 grit size) on a pin-on-disc machine at a speed of 0.5 m/s under nominal normal loads varying from 20 to 80N for 25 s. The main arguments are developed using X-ray diffraction data in the 2θ range of 25° to 36° and supported by scanning electron microscopy. This range includes the most intense reflection $(111)_T$ from the tetragonal (T) phase and the first two intense reflections, that is $(\bar{1}11)_M$ and $(111)_M$ from the monoclinic (M) phase.

3. Results and discussion

An occurrence of an intermediate phase designated as X (between tetragonal and monoclinic) is observed after the cutting process as a shoulder in the main tetragonal peak. Etching brings about a tetragonal to intermediate to monoclinic (T→X→M) transformation. Removal of the intermediate phase by etching is accompanied by an increase in the monoclinic phase.

Scanning electron microscopy reveals the presence of pits on the cut surface which become numerous with etching. The occurrence of pits is considered to be due to the local volume change caused by transformation of tetragonal to intermediate phase which the material is not able to sustain without cracking. Prolonged etching causes severe pitting and gives rise to a loosely bound granular surface. The hardness of the cut surface is found to be greater than the cut and etched surface which indicates the presence of monoclinic on the cut and etched surface.

On abrasion, the wear rate of the cut surface is found to be lower than that of the cut and etched surface at all loads. The X-ray diffraction of the worn surfaces shows the presence of the tetragonal and the intermediate phases on the surface along with a small amount of monoclinic. The relatively high wear rate of the cut and etched surface is considered to be due to the initial presence and subsequent removal of a monoclinic-rich surface layer, which is highly pitted. Increasing the etching time increases the wear rate possibly due to the progressive accentuation of monoclinic enrichment and morphological degradation of the initial surface layers.

It is inferred from the present study that, in the case of 3Y-TZP, processes such as cutting and abrasion wherein tangential stresses are applied lead to the formation of the intermediate phase and etching changes the intermediate phase to the monoclinic phase.

References

1. GARVIE, R. C., HANNINK, H. J. AND PASCOE, R. T. — Ceramic steel?, *Nature* (Lond.), 1975, **258**, 703–704.
2. REECE, M. J., TELLOW, P. L. AND GALIOTIS, C. — Phase transformation around indentations in zirconia, *J. Mater. Sci Lett.*, 1972, **11**, 575–577.
3. MARSHALL, D. B., JAMES, M. R. AND PORTER, J. R. — Structural and mechanical property changes in toughened Mg-PSZ at low temperatures, *J. Am. Cer. Soc.*, 1989, **72**, 218–227.

Thesis Abstract (Ph.D.)

Some electrical characteristics of grain boundaries in cast polysilicon by P. R. Suresh

Research supervisor: M. Satyam
Department: Electrical Communication Engineering

1. Introduction

Polycrystalline silicon, widely known as polysilicon, is finding increasing application in the field of large area devices like solar cells. Among the various types of polysilicons available, cast polysilicon is attracting the attention of many investigators. This is mainly due to the simple process involved in the preparation of this material compared to the relatively complicated process used for the preparation of single-crystal silicon. This makes it a cheaper alternative for fabricating electronic devices. But the grain boundaries (GBs) that are present in this material act as traps and recombination centres for the carriers, thus deteriorating the performance of the devices fabricated on polysilicon[1,2]. In order to improve the performance of these devices, investigations on the electrical behaviours of GBs from the point of charge storage and charge transport across them have been carried out and some suggestions have been made to reduce the defects at GBs.

2. Experimental

The samples chosen for the present studies were cut from p-type cast polysilicon wafers supplied by Wacker Chemitronic. The samples were first cleaned in acetone and then etched in a mixture of $5HF/3HNO_3/3CH_3COOH$ solution. Ohmic contacts were made by depositing high-purity aluminium dots on either of the GB of interest, on one side of the wafer. This was followed by sintering at 450°C for 10 min. Capacitance–voltage (C-V) and current–voltage (I-V) characteristics of GBs were measured using an automatic C-V plotter

supplied by the Material Development Corporation and a Keithley source measure unit (SMU236), respectively. In some cases, the capacitance of GBs was measured using an LCR bridge.

In addition to this, the effect of temperature on I–V and C–V characteristics of GBs in polysilicon has been investigated. Also, the effect of annealing and aluminium diffusion into polysilicon at various temperatures and for various durations have been studied.

3. Results and conclusions

It has been found that the I–V and C–V characteristics of GBs show a dependence on the polarity of the applied voltage. A model has been developed to understand the observed results by taking the variation in carrier concentration from grain to grain into account. In this model, it has been assumed that the carrier transport across GBs is by thermionic emission and also that the trap states at the GBs are situated at a single energy level. The effect of tunneling from the GB trap states into the conduction band of the reverse biased grain has been considered at higher voltages. The computed I–V characteristics of GBs show the same general features as that of the measured I–V characteristics. The effect of various parameters like carrier concentrations in the grains forming the GB, the density of grap states at the GB and the position of these trap states in the forbidden gap on I–V characteristics of GBs have been discussed in detail.

The C–V characteristics of GBs in cast polysilicon have been observed to exhibit various shapes. This has been explained as due to the change in total depletion layer width associated with GBs as a function of bias. The calculations performed indicate that depending upon the value of trap density, carrier concentrations and the trap energy level, the total depletion layer width associated with GBs may increase or decrease depending upon the bias. The capacitance of GBs follows these changes as a function of bias and hence C–V characteristics exhibit various shapes[3]

The observed increase in the capacitance of GB and current through the GB as temperature increases have been attributed to the reduction in the density of filled traps as the temperature increases. The computed C–V and I–V characteristics as a function of temperature show the same trend as that of the measured characteristics.

The present investigation shows that annealing of polysilicon samples at moderately high temperatures (450°C and below) increases the capacitance of GBs and current through the GBs, but annealing of this material at high temperatures (600°C) tends to reduce these values. From the measured values of GB capacitance, calculations of trap state density at the GB has been made both before and after annealing of these samples. These calculations suggest that the density of interface trap states decreases after annealing at moderately high temperatures whereas it increases after annealing at higher temperatures.

It has been observed that aluminium diffusion into polysilison at 450°C and below decreases the capacitance of GBs and current through the GBs whereas aluminium diffusion at 700°C increases the values of these parameters. Based on the calculations made, it has been concluded that aluminium acts as a trap centre when diffused at moderately high temperatures but it acts as a dopant or as a passivating agent or as both when diffusion at high temperatures into polysilicon. In addition, a combined treatment of aluminium diffusion at 700°C and annealing at 450°C has been found to act as a complementary technique to significantly reduce the density of interface trap states at the GBs in silicon. These results suggest the possibility of getting enhanced performance from devices fabricated on polysilicon.

References

1. GHOSH, A. K., FISHERMAN, C. AND FENG, T. — *J. Appl. Phys.*, 1980, **51**, 446–454.
2. GROVENER, C. R. M. — *J. Phys. C., Solid St. Phys.*, 1985, **18**, 4079–4119.
3. SURESH, P. R., RAMKUMAR, K. AND SATYAM, M. — *J. Appl. Phys.*, 1991, **69**, 8217–8221.

Thesis Abstract (Ph.D.)

Impedance parameters of sealed batteries by S. A. Ilangovan

Research supervisor: S. Sathyanarayana
Department: Inorganic and Physical Chemistry

1. Introduction

The expanding role of primary and secondary batteries in modern society has prompted the evolution of a variety of new and improved battery systems in recent years A fundamental characterization of battery operation requires impedance parameters such as charge transfer resistances and double layer capacitances of the cathodes and anodes individually, as well as the internal resistance of the battery Evaluation of these parameters is particularly important with the advent of sealed batteries, since access to the individual electrodes or the electrolyte is quite difficult without destroying the battery

In a recent attempt[1] on the 'nondestructive characterization of sealed lead–acid battery cells with electrochemical impedance spectroscopy', several difficulties have been pointed out, and only charge transfer resistances, as a sum, as well as double layer capacitances, also as a sum, of anodes and cathodes could be determined

The problem of nondestructive determination of resistance and reactance parameters of cathodes, anodes as batteries has not been solved so far, the present study is focused on offering a solution to it

2. Theory

At the outset, a generalised equivalent circuit for the battery impedance is proposed which includes inductive capacitive and resistive elements with some of these being considered variable with potential and duration of the test.

The situation is simplified by considering well-defined and verifiable conditions of a proposed galvanostatic non-destructive test (GNDT) method[2] In doing so, experimental conditions have to be chosen judiciously so as to (i) eliminate diffusion impedance as well as series inductive reactances, and (ii) ensure that the change in the state-of-charge (SOC) of the battery is negligibly small during the experiment The simplified equivalent circuit (Fig 1) has five constant impedance parameters (R_i, $R_{t,1}$, $R_{t,2}$, $C_{d,1}$ and $C_{d,2}$) under the GNDT conditions characterizing the battery impedance completely in terms of contribution from the cathodes, the anodes, the separator electrolyte and the interelectrode space

The governing equation for the voltage–time discharge transient of a battery corresponding to the equivalent circuit of Fig 1 is:

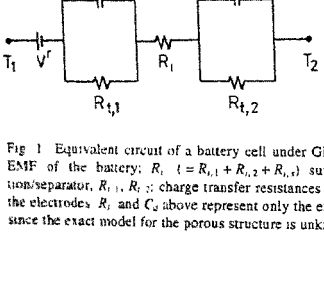

Fig 1 Equivalent circuit of a battery cell under GNDT conditions. T_1, T_2, battery terminals; V^r = reversible EMF of the battery; R_i ($= R_{i,1} + R_{i,2} + R_{i,s}$) sum of ohmic resistances of cathode, anode and solution/separator, $R_{t,1}$, $R_{t,2}$: charge transfer resistances of the electrodes; $C_{d,1}$, $C_{d,2}$: double layer capacitances of the electrodes R_i and C_d above represent only the effective values for the porous electrodes in the battery cell since the exact model for the porous structure is unknown.

$$V' - V = IR_i + IR_{t,1}[1 - \exp(-t/\tau_1)] + IR_{t,2}[1 - \exp(-t/\tau_2)] \quad (1)$$

where V' is the reversible (equilibrium) EMF of the battery at the given SOC, V, the voltage at time t after initiating a discharge with the test current I; τ_1 ($= R_{t,1} C_{d,1}$) and τ_2 ($\approx R_{t,2} C_{d,2}$) are the time constants of the charge-transfer-controlled processes at the cell cathode and cell anode, respectively. If the time constants of the two relaxation processes are widely separated, *i.e.*, $\tau_1 >> \tau_2$, there is no difficulty in solving eqn (1) with experimental data, but such a situation cannot be assumed without adequate reasons and is unlikely to be always valid in practical systems.

3. The data analysis procedure

The general case of comparable time constants is important and is hence taken up for analysis in this study.

It is first demonstrated that an algebraic approach to solve eqn (1) for the five impedance parameters by considering the first to fourth derivative at the origin ($V = V'$, $t = 0$) is fraught with such serious errors when using actual measurements of V *vs* t, as to render the solutions useless from a practical point of view.

A new robust data-processing technique[2] is therefore necessary and is developed in this study. The essence of the technique is to delineate the time domain for the longer relaxation process by an initial graphical approximation procedure, and then evaluate the contributions of the two relaxation processes individually by a computerised iterative operation which identifies the solutions for all the impedance parameters within any preset error limits. The correctness of the proposed method is first verified extensively by simulation studies, and then applied to sealed lead–acid, nickel–cadmium, alkaline Zn–MnO_2 and nonaqueous Li–MnO_2 batteries at various SOCs.

4. Experimental details

To meet the fundamental requirements of GNDT experiments, a test set-up shown in Fig. 2 has been successfully developed to accurately measure the minute changes in battery cell voltage at short time intervals during galvanostatic discharge at an extraordinary low rate.

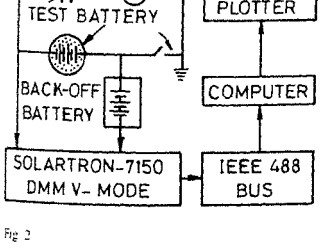

Fig. 2

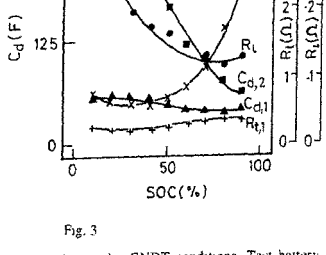

Fig. 3

Fig. 2 Test set-up (schematic) for digital recording of V–t transient under GNDT conditions. Test battery: Battery (or battery cell) under study; DVM: Solartron-7150 digital multimeter in V_{dc} mode (200 mV range, ±1 μV resolution); R: resistance adjusted to give desired constant current when switch is closed. Back-off battery: similar to test battery, with about 90% state of charge, kept on open circuit for about 50 h prior to the test.

Fig. 3 Plot of impedance parameters of cathode, anode and solution/separator against SOC for sealed lead–acid battery (Yuasa 6 V, 4 A h) at 29.7 ± 0.1°C.

A digital multimeter used in the voltage mode and controlled by a computer was used to acquire data points at every 0.4 s for a total duration of 120 s.

Sealed lead–acid batteries (Yuasa 6 V, 4 A h), nickel–cadmium (Saft 1.2 V, 21 A h), alkaline Zn–MnO_2 (Duracell 1.5 V, 5.3 A h) and nonaqueous Li–MnO_2 (Duracell 3.0 V, 1.3 A h) were used for the test. The discharge test was begun under GNDT conditions for each battery separately, by drawing a predetermined and sufficiently small test current ($< C_A/700$ A) using the test battery itself as the source and an appropriate series resistance (R) to control the current at the desired level. The battery voltage was backed-off by a stabilized battery of the same kind at 90% SOC, in order to utilize the full sensitivity of the digital multimeter.

Considerable care was found necessary in regard to the control of ambient temperature (within ±0.1°C), wiring precautions, software development for data acquisition and attainment of the desired SOC of the battery. Under the same conditions, voltage–time discharge transients of the above-mentioned systems were recorded as a function of SOC.

5. Conclusions

The results, illustrated typically for sealed lead–acid batteries in Fig. 3, permit, for the first time, an insight into the values of the impedance parameters of individual electrodes and the internal resistance of sealed batteries at different SOC. It is surmised that

(i) the above investigations lead to the significant conclusion that the individual values of all the five impedance parameters, namely, charge transfer resistance of the cathode and of the anode, as well as double layer resistance of the cathode and the anode, and the internal resistance of batteries can be determined accurately by the proposed GNDT method,

(ii) the model and data analysis are not restricted either to linear approximations in the time domain or to well-ordered data, the nonlinear-in-time model retains all the important impedance parameters of real system while the data analysis leads logically to unique and reliable values of the electrode impedance parameters and cell internal resistance, from measurements on real systems,

(iii) the diffusion impedance which usually distorts the data and complicates the analysis can be rendered negligible by adopting suitable (and verifiable) conditions,

(iv) the effects due to any series inductance of battery cells, which render ac impedance measurements of doubtful value, can be eliminated by the galvanostatic test mode,

(v) spurious effects due to switching transients can be eliminated since the data made use of for analysis are those obtained well after the decay of these transients,

(vi) the technique provides, for the first time, a fundamental framework for the evaluation, design improvement, and development strategies for battery systems since the impedance parameters are obtained as discrete contributions from cathode, anode and the electrolyte/separator components of sealed batteries,

(vii) the SOC of sealed lead–acid batteries is best predicted through the double layer capacitances of cathode,

(viii) the SOC of nickel–cadium battery is best predicted through the relaxation time of cathode,

(ix) the SOC of alkaline zinc–manganese dioxide and of nonaqueous lithium–manganese dioxide primary cells is not predictable through any of the impedance parameters or the relaxation times, and

(x) electrocatalysis of the positive electrode reaction is the preferred direction for an improved electrochemical design of the above battery systems.

References

1. Rohleder, P. R., Halliop, E., Verville, G. and Smit, J. — *J. Power Sources*, 1990, **32**, 261–270.
2. Elangovan, S. A. and Satyanarayana, S. — *J. Appl. Electrochem.*, 1992, **22**, 456–463.

Thesis Abstract (Ph.D.)

SVD-based criteria for detection of the number of damped/undamped sinusoids in noise and their parameter estimation by L. S. Biradar

Research supervisor: V. U. Reddy
Department: Electrical Communication Engineering

1. Introduction

The problem of estimating the parameters of superimposed damped/undamped sinusoids in the presence of white noise arises in many practical applications. Further, in practice, we have to attempt this problem with a small number of data samples and possibly at low signal-to-noise ratio. These two constraints, imposed by practical considerations, make the problem more difficult.

Several approaches based on both linear nonlinear least squares formulations have been recently proposed for estimating the parameters. Among the linear least squares-based approaches, modified linear prediction methods 1 and total least squares method 2 have received a lot of attention. In these methods, known as singular value decomposition (SVD)-based methods, we require the knowledge of the number of sinusoids which, in general, is not available a priori.

Among the nonlinear least squares-based approaches, iterative quadratic maximum likelihood (IQML)[3] and alternating projection (AP)[4] algorithm have received considerable attention. The AP algorithm is computationally intensive, and in its basic form its convergence is slow.

2. Results and discussion

Following the information theoretic approach to model selection, *AIC* and *MDL criteria have been developed* for detecting the number of damped/undamped sinusoids. Using the assumptions similar to those made by others in the context of such problems, an analytical framework has been developed for analysing the performance of the criteria. The development of the criteria and analysis makes use of certain approximations which become better for large signal-to-noise ratio (SNR). The detection criteria are matched to the SVD-based methods so well that additional computations required over and above other needed for SVD calculation are marginal. The performance of the proposed criteria is compared with that of a recently suggested criterion by Fuchs[5] using simulations, and the results show that both the methods perform similarly. But, Fuchs method is computationally more expensive. Further, the usefulness of the analysis is checked by comparing the theoretically predicted values of probability of detection with those obtained from simulation, and the results show good agreement between the two even at moderate SNR.

The nonlinear least squares problem, in general, involves multidimensional maximization (or minimization) which is computationally expensive. The AP algorithm[6] reduces the multidimensional maximization problem into a sequence of simpler one-dimensional maximizations. To apply the Newton–Raphson search technique so as to speed up the convergence of the AP algorithm, closed-form expressions for gradient and Hessian functions of the objective function are developed. The performance of the Newton-based AP algorithm is compared with that of recent techniques such as total least squares and *IQML methods using extensive* simulations. The results show that the threshold SNR of the AP method is lower than that of others while the estimation accuracy of all the methods away from the threshold is nearly the same.

References

1. Tufts, D. W. and Kumaresan, R. — Estimation of frequencies of multiple sinusoids: making linear prediction perform like maximum likelihood, *Proc. IEEE*, 1982, **70**, 975–989.

2. Rahman, M. A. and Yu, K. B. — Total least squares approach for frequency estimation using *linear prediction*, *IEEE Trans.*, 1987, **ASSP-35**, 1440–1454.

3. Bresler, Y. and Macovski, A. — Exact maximum likelihood parameter estimation of superimposed exponential signals in noise, *IEEE Trans.*, 1986, **ASSP-34**, 1081–1089.

4 ZISKIND, I AND WAX, M Maximum likelihood localization of multiple sources by alternating projection, *IEEE Trans*, 1988, **ASSP-36**, 1553–1560

5. FUCHS, J J Estimating the number of sinusoids in additive white noise, *IEEE Trans*, 1988, **ASSP-36**, 1846–1853

Thesis Abstract (Ph.D.)

Knowledge based systems for diagnostic problem solving of power systems and hvdc networks by K. Shanti Swarup

Research supervisor: H. S. Chandrasekharaiah
Department: High Voltage Engineering

1. Introduction

Fault detection and diagnosis is an important area of research for operational reliability of a power system Conventional approaches to fault diagnosis involve the identification of a fault based on observed signals from relays and circuit breakers. This task tends to be complex for a large interconnected network, where the heuristics and experience of the operator together with the technical characteristics of the power system play an important role during the process of diagnosis and decision making The complexity of this task increases with the occurrence of simultaneous, multiple and unknown faults experienced in real-world situations. Hence there is a need for the feasibility study and identification of different approaches for diagnostic problem solving of power systems to meet the above-mentioned requirements This requires the identification of the discriminatory performance and diagnostic inference to be obtained by different available approaches for problem solving In the recent past, the task of fault detection, diagnosis and decision making has been achieved with the help of new information (*symbolic*) processing methods termed as 'knowledge-based systems', consisting mainly of emulating the diagnostic and decision-making capability of the human expert by capturing the empirical (*and experiential knowledge*) and representing in it a form suitable for symbolic processing[1,2] Feasibility of application, suitability and solution requirement are of utmost importance in the selection of particular approach for problem solving

2. Diagnostic problem solving approaches

This thesis presents the identification and problem formulation of various qualitative and quantitative methods for diagnostic problem solving of power systems[3]. In this thesis, diagnostic problem solving (*consisting mainly of representing the problem to be solved, defining strategies for searching for the solutions and defining heuristics to guide these strategies*), has been classified into the following approaches of artificial intelligence (AI), pattern recognition (PR) and knowledge-based pattern recognition (KBPR). Problem formulation and knowledge (and data) representation and implementation aspects of each of these approaches is discussed and presented in detail.

2.1. *Artificial intelligence approach*

In the artificial intelligence approach, two basic methods of shallow and deep reasoning are considered Production rules are employed in the shallow approach, to represent empirical relations between the observations (symptoms) and fault conditions. The empirical (experiential) knowledge of the expert is represented in the form of IF<conditions> THEN <actions>[4] The knowledge base consists of rules and facts about the normal and abnormal operating state of the power system. In the case of power system fault diagnosis, the input to the diagnostic expert system consists of the signals of the relays and circuit breakers of the power system The diagnostic expert systems provide information about the faulted component of the power system along with its probability of occurrence. In the case of high-voltage direct current (hvdc) system diagnosis, the input to the

diagnostic expert system consists of the rules describing the various on/off sequences of the periods of conducting thyristors, pulse-zone periods and voltage zone periods, respectively, in addition to the ac and dc characteristics. The diagnostic expert system provides information about the cause of the fault, its type and location. The instance of fault occurrence, its duration and severity can be obtained from the diagnostic conclusions.

The deep reasoning approach, also termed as model-based reasoning, qualitative reasoning (simulation) and model-based qualitative reasoning[4,5], provides an insight into the interaction of basic components of the power system. The deep reasoning approach to fault diagnosis provides an efficient means for the description of the system based on its structure and behaviour[5]. It is possible to detect and identify the basic components malfunctioning in the system through a procedure termed as constraint propagation. The observed and predicted behaviour of operation of the power system are presented as input to the model-based diagnostic system. Diagnostic reasoning is performed based on the discrepancy between the observed and predicted behaviour. This procedure basically follows a *hypothesize and test* approach for the generation and evaluation of hypothesis.

2.2 *Pattern recognition approach*

Pattern recognition approach to diagnostic problem solving consists of classification of the input patterns into one of the fault conditions[6,7]. Pattern classification and discrimination, using Baye's decision theory and linear discriminant functions, are employed for the task of fault classification and analysis.

2.2.1. *Bayesian approach*

The Bayesian approach to fault classification consists of calculating the a priori, a posteriori, and *joint conditional probabilities* of the input pattern and its corresponding class based on the information on the signals of relays and circuit breakers of the power system. The input to the pattern recognition system consists of calculating the probability distributions based on the qualitative behaviour of the power system. The output consists of joint a posterior probabilities of all the components of the power system and performing fault discrimination based on the identification of the component with the largest posterior probability. This approach also provides information regarding the fault probabilities of other likely faulted components of the power system.

2.2.2. *Discriminant functions*

The discriminant analysis approach to diagnosis of representing the system as a function (linear or quadratic) of the signals (tripping) of the relays, circuit breakers, and components of the power system. The task of the pattern recognition system is to map the input pattern to one of the possible fault conditions, which are usually the components of the power system. The output consists of the classes (normal or faulted) of the components of the power system.

The advantage of pattern recognition approach to diagnostic problem solving is that the process of fault classification and discrimination can be performed online. The pattern recognition approach performs only statistical pattern classification and there is a need for representing the information content of the input pattern. Structural pattern-recognition or pattern-directed systems can be effectively used for this purpose.

2.3. *Artificial neural networks*

Artificial neural networks (ANNs) are generally considered as the adaptive pattern recognition approach to diagnostic problem solving[3,8]. ANNs can be used to represent the inherent nonlinear relationship of the system and can be also used to learn patterns of activation. The neural network diagnostic system can be trained offline and used online to perform the tasks of learning, generalization and abstraction. The input to the neural network diagnostic system consists of the signals of the relays of the circuit breakers of the qualitative behaviour of the power system, while the output consists of the probability of the faulted component. The characteristics of the neural network have been obtained for different operating conditions for the ac and dc power systems.

2.4. *Knowledge-based pattern recognition*

Researchers in the field of artificial intelligence and cognitive psychology have been working on integrating the inherent advantages of artificial intelligence and pattern recognition approaches for efficient problem

solving. This has resulted in the identification and development study of a new approach termed as *knowledge-based pattern recognition* (KBPR)[9]. Feasibility study of KBPR for diagnosis problem solving has resulted in the identification of the following approaches, namely, pattern-directed expert system, inductive inference and pattern-directed inference systems.

2.4.1. *Pattern-directed expert system*

Pattern-directed expert system essentially consists of the rule-based representation of input patterns Salient features of the (time-varying continuous) input pattern in terms of time instance, duration, severity and (fault) recovery are explicitly represented by this approach. Diagnostic problem solving is achieved by the process similar to pattern matching. In the case of fault diagnosis of hvdc systems, the knowledge base of the pattern-directed expert system consists of the time-varying patterns of the conducting thyristors, pulse-zone periods and voltage-zone periods represented as IF–THEN rules.

2.4.2. *Inductive inference*

Inductive inference, also termed as the artificial intelligence approach to pattern recognition, basically consists of the construction of the decision tree based on the features of the input pattern and class membership. Inductive inference using the ID3 algorithm is employed for diagnostic problem solving of power systems and hvdc networks. The inductive inference diagnostic system provides information about the probability of the fault component in the form of a decision tree. Probability of other components can be obtained from the next level of the decision tree.

2.4 3. *Pattern-directed inference system*

The pattern-directed inference system combines the principles of pattern-directed expert system and inductive inference for diagnostic problem solving. Pattern-directed inference system consists mainly of pattern-directed modules, which are responsible for detecting various situations and responding appropriately to them Pattern matching, as performed by the pattern-directed module, involves reading information into a data structure and then checking to see if it matches a particular template associated with the pattern-directed module. The knowledge base of the pattern-directed system contains hierarchical categorization of faults, manifestations, and inter-relationships between manifestations and diagnosis. Each fault category of classification is characterized by a set of pattern vectors which are described in terms of a group of associated manifestations

Feasibility of application of these approaches has been carried for two case studies of discrete data set (ac power system) and continuous data set (high-voltage direct current system) Suitability of application of these approaches is presented in Section 3

References

1 SAKAGUCHI, T. AND WOLLENBERG, B F. Artificial intelligence and the control of electrical power systems, *Proc. IEEE*, 1987, 1678–1685.

2 TALUKDAR, S N. AND CARDOZO, E. Artificial intelligence techniques in power system operation, *EPRI Report*, EL-4323, 1987

3 PAO, Y. H. *Adaptive pattern recognition and neural networks*, 1989, Addison-Wesley

4. BARKTO, I. *Prolog programming for artificial intelligence*, 1988, Addison-Wesley.

5. DAVIS, R. Diagnostic reasoning based on the structure and behaviour, *Artif. Intell*, 1984, **24**, 347–410.

6 REGGIA, J AND PENG, Y *Abductive reasoning for diagnostic problem solving*, 1991, Springer Verlag.

7. ISHERMANN, R. Process fault detection based on modelling and parameter estimation methods–A survey, *Automatica*, 1984, **20**, 187–404

3. Comparative analysis of knowledge-based approaches for diagnostic problem solving

Approach	Methodology	Feature	Characteristics	Inference
Artificial intelligence	Rule-based	Shallow reasoning	Captures empirical relations and experiential knowledge	Mapping symptoms to fault conditions
	Model-based	Deep reasoning	Reasoning based on the description of the structure and behaviour	Discrepancy detection based on the observed and predicted behaviour of the physical system
	Model-based qualitative reasoning	Qualitative behaviour and analysis of systems	Casual and functional relation between components of the system	Detection and evaluation of violated constraints
Pattern recognition	Bayesian Decision Theory	Probabilistic functions and pattern classification	Statistical pattern recognition. Calculation of the probability of the components of the system	Probability estimates of the pattern vector and class membership
	Discriminant functions	Pattern classification and discriminant analysis	Feature selection, extraction and classification	Mapping feature space to decision space
Artificial neural networks	Back propagation training algorithm	Pattern classification and feature mapping	Nonlinear system representation	Behavioural pattern matching
Knowledge-based pattern recognition	Pattern-directed expert system	Rule-based representation of signals of input patterns	Pattern-directed inference of signals	Pattern matching of identical antecedents
	Inductive inference	Artificial intelligence approach to pattern recognition	Decision tree construction and analysis	Entropy minimization and fault probability estimation
	Pattern-directed inference system	Integration of pattern-directed expert system and inductive inference	Feature extraction of the input data to select pieces of code and trigger activities	Selection and activation of pattern-directed modules that change the data elements

ANDERSON, J. A AND ROSENFIELD, E. *Neuro-computing: Foundations of research*, 1988, MIT Press, Cambridge.

WATERMAN, D. A. AND HAYESROTH, F. *Pattern directed inference systems*, 1978, Academic Press.

Thesis Abstract (M. Sc. (Engng))

Analysis and simulation of ice storage air-conditioning systems by H. V. Pradeep

Research supervisor: M. V. Krishnamurthy
Department: Mechanical Engineering

1. Introduction

Ice storage air-conditioning system is a form of distributed load management where ice is made during off-peak periods and used to cool the building during peak periods. The concept is relatively recent and such systems have been installed only since the last decade or so. Although many investigators have studied the performance of actual thermal storage systems, only a few investigations present any theoretical analysis of these systems. Analysis of a thermal storage system helps in the optimal design of the system This depends on the building type, cooling load profiles, location of the system, etc. Also, the performance of the system under varying operating conditions can be analysed

Silver *et al.*[1] have developed component models and a software package for the simulation of ice-on-coil type ice builders. The program can be used to simulate several ice storage system configurations and control strategies. However, the software cannot model glycol or brine systems, systems employing direct expansion coils and systems with thermostatic control. Load prediction capability is also not incorporated

Bhansali and Hittle[2] have discussed the use of cold air distribution systems in conjuction with a full ice storage as a means to reduce peak power and energy consumption. Evaporative condensers were chosen with the ice storage system. They have not considered partial ice storage system which will have the advantage of lower initial system cost due to the reduced system capacity, efficient utilization of the compressor and electrical load levelling.

Musgrove[3] has developed a model to simulate and optimize the operation of ice storage systems The model employs capital and operating cost data to optimize the size of chiller and ice storage for an annual operating cycle taking into account several different seasonal load conditions But in this analysis, systems with air-cooled condensers are not considered. Also, no diurnal and seasonal variation in the system performance is considered

From all the above literature it is observed that a detailed theoretical analysis of ice storage systems has not been carried out though many investigations have been performed on already existing systems. Some theoretical analyses performed on the system are based on the assumptions of constant condensing temperature and *do not consider the diurnal variations of ambient conditions. Thus the results obtained from* such analysis would not be realistic enough. Also, investigations on ice storage systems employing air-cooled condensers or thermostatic control have not been carried out

2. Model

A detailed analysis of ice storage air-conditioning systems taking into consideration the diurnal changes in the ambient conditions, variations in the condensing temperature with time, ice storage strategies like partial, full and no ice storage, is presented. The analysis incorporates thermostatic control and transient cooling load calculations.

The ice storage system consists of evaporator, compressor, condenser, expansion device and ice storage tank (Fig. 1). There are two circuits in the system, namely, the refrigerant circuit and the brine circuit. In the present study, R22 and ethylene glycol of 30% concentration are chosen as the refrigerant. The evaporator temperature varies depending on whether the system is used for making ice or for cooling the conditioned space. The system can operate in the following three modes:

- Building cooling mode
- Ice-making mode
- Combined mode

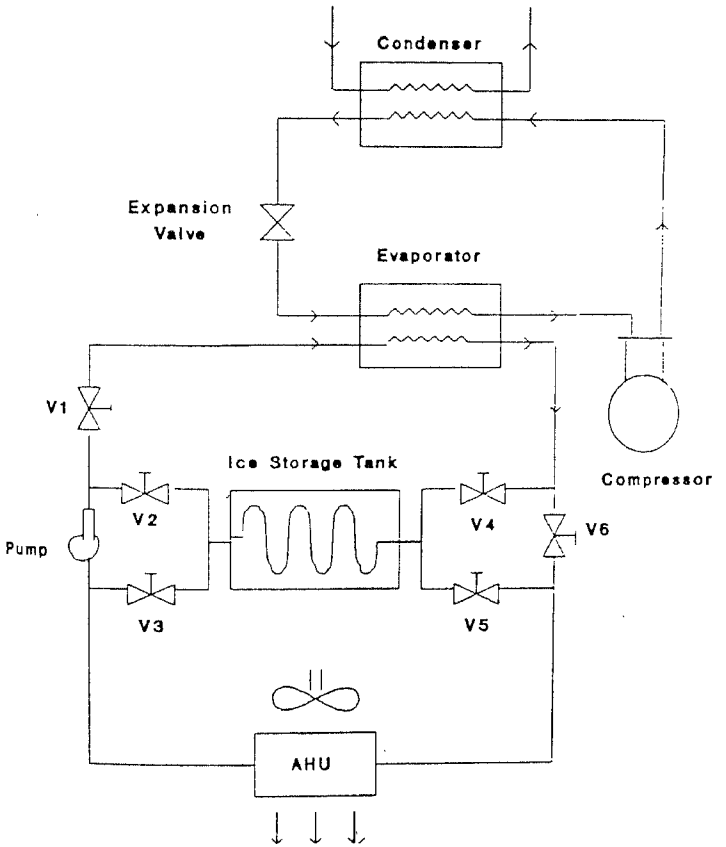

Fig. 1 Schematic diagram of the ice-storage air-conditioning system.

In the building cooling mode, the brine solution is circulated through an air-handling unit which cools the conditioned space. The warm brine solution from the air-handling unit flows either only to the ice storage tank or only to the evaporator or a part of it to the storage tank and the remaining to the evaporator depending on the storage strategy employed which may be full, partial or no ice storage where it is cooled.

In the ice-making mode, the brine is cooled in the evaporator and flows to the ice storage tank where it freezes water into ice. When the required quantity of ice is made, the compressor is switched off.

In the combined mode, the evaporator is simultaneously used for ice-making and cooling purposes. A part of the cold brine solution from the evaporator flows to the ice storage tank for making ice and the remaining to the air-handling unit to provide air-conditioning.

A generalized computer program ISAC is written for the analysis and simulation of ice storage air-conditioning systems The program calculates the incident solar load, cooling load variations over a day and the properties of refrigerants at various state points, sizes the refrigeration system components, brine-to-water heat exchanger and ice storage tank, simulates the system under off-design operating conditions, different storage strategies and the performance of the system with and without thermostat.

3. Results and discussion

By comparing the energy requirements for systems with partial, full and no ice storage (Tables I–III), it can be seen that generally the increase in energy consumption with ice storage is more pronounced in systems employing water-cooled condenser, which is mainly because of the lesser variations in the wet-bulb temperature

Table I

Results of simulation for New Delhi for the month of May

Condenser	Storage	Mode	Compressor capacity			Compressor power			Compressor ontime (h)
			Min. kW	Max. kW	Total kWh	Min. kW	Max. kW	Total kWh	
Air-cooled condenser	Partial storage	Cooling	1.44	1.58	20.8	0.2	0.285	3.46	13 85
		Ice making	1.04	1.12	11.05	0.2	0.26	2.27	10.15
	No storage	Cooling	2.22	2.43	31.95	0.29	0.42	5.12	13.8
	Full storage	Ice making	2.2	2.36	32.26	0.39	0.49	6.03	14.0
Water-cooled condenser	Partial storage	Cooling	1.51	1.54	19.74	0.17	0.20	2.44	13.0
		Ice making	1.08	1.09	10.54	0.17	0.18	1.67	9 69
	No storage	Cooling	2.32	2.37	30.37	0.25	0.29	3.59	14.5
	Full storage	Ice making	2.19	2.27	32.16	0.34	0.37	5.01	14.3

Table II

Results of simulation for Jodhpur for the month of May

Condenser	Storage	Mode	Compressor capacity			Compressor power			Compressor ontime (h)
			Min. kW	Max. kW	Total kWh	Min. kW	Max. kW	Total kWh	
Air-cooled condenser	Partial storage	Cooling	1.65	1.82	25.0	0.24	0.35	4.50	14.61
		Ice making	1.10	1.24	10.65	0.24	0.3	2.43	9.08
	No storage	Cooling	2.36	2.61	35.55	0.32	0.49	6.17	14.5
	Full storage	Ice making	2.36	2.51	34.20	0.43	0.54	6.81	14.0
Water-cooled condenser	Partial storage	Cooling	1.72	1.75	24.94	0.20	0.23	3.08	13.4
		Ice making	1.15	1.16	10.57	0.19	0.20	1.79	9.15
	No storage	Cooling	2.46	2.51	35.25	0.29	0.33	4.45	14.23
	Full storage	Ice making	2.33	2.40	34.11	0.37	0.40	5.35	14.31

Table III

Results of simulation for Madras for the month of May

Condenser	Storage	Mode	Compressor capacity			Compressor power			Compressor ontime (h)
			Min. kW	Max. kW	Total kWh	Min. kW	Max. kW	Total kWh	
Air-cooled condenser	Partial storage	Cooling	1.40	1.48	18.6	0.2	0.25	3.02	13.0
		Ice making	1.06	1.08	10.13	0.2	0.21	1.95	9.46
	No storage	Cooling	2.16	2.39	28.78	0.31	0.37	4.49	13.0
	Full storage	Ice making	2.2	2.25	30.43	0.40	0.44	5.66	13.7
Water-cooled condenser	Partial storage	Cooling	1.39	1.40	18.09	0.21	0.22	2.72	13.0
		Ice making	1.01	1.03	10.10	0.205	0.21	2.06	9.92
	No storage	Cooling	2.14	2.16	27.94	0.31	0.32	4.04	13.0
	Full storage	Ice making	2.10	2.13	30.41	0.41	0.43	6.01	14.4

It can also be seen that the increase in energy consumption is very small in places with large day-and-night temperature differential like Jodhpur and for partial ice storage systems it is generally small for all places. The increase in energy requirement is reduced by employing partial storage mainly because only a part of the cooling load is taken by ice storage and also ice is produced only during the time of the day when the ambient temperature is the lowest. This is not entirely possible with systems employing full storage because a part of the ice will have to be produced during morning time when the ambient temperature is high.

By employing partial storage, it can be seen that the electric power demand is considerably reduced thus helping in electric load levelling. By employing full ice storage, the electric power demand is shifted from on-peak to off-peak periods which also helps in the electric load levelling.

Also, it can be seen from Table IV that in the case of a system which does not employ ice storage, the compressor will operate only for 13.5 h and will remain idle the rest of the time, while for a system employing partial storage, the compressor will be idle for only about on hour a day. Thus, there is an efficient capacity utilization of the refrigerating system by employing ice storage.

4. Conclusions

Some of the conclusions obtained from the analysis are:

- By employing ice storage, the system size can be reduced by nearly 30–35% resulting in reduced initial cost.
- Partial ice storage systems reduce the peak compressor power requirement thereby reducing the electric power demand.
- Since the variation in dry-bulb temperature is more than the wet-bulb temperature, systems with air-cooled condenser are more advantageous.
- By employing partial ice storage, the ontime period of the compressor can be considerably increased resulting in the optimum utilization of the compressor.

Table IV

Compressor ontime (in hours)

	Storage	New Delhi	Jodhpur	Madras
Water-cooled condenser	No	14.5	14.2	13
	Partial	22.7	22.6	22.9
Air-cooled condenser	No	13.8	14.5	13
	Partial	24	23.7	22.5

References

1. SILVER, S. C., JONES, J. W., PETERSON, J. L. AND HUNN, B. D. CBS/ICE: A computer program of simulation of ice storage systems, *ASHRAE Trans.* (1), 1989, 1206–1213.
2. BHANSALI, A. AND HITTLE, D. C. Estimated energy consumption and operating cost for ice storage systems with cold air distribution, *ASHRAE Trans.* (1), 1990, 418–427.
3. MUSGROVE, A. R. DE L. Istore–A model to simulate and optimize the operation of ice storage air-conditioning systems, *Int. J. Energy Res.*, 1990, **14**, 199–208.

Thesis Abstract (Ph.D.)

Analysis of thick orthotropic and laminated circular cylindrical shells by B. Sreehari Kumar

Research supervisor: K. Chandrashekhara
Department: Civil Engineering

1. Introduction

Structural applications of single and multilayered circular cylindrical shell of revolution and shell panel, made of composite material, in the field of aerospace, transportation, medical and building industry are ever on increase due to their high modulus to low density material properties. In recent years, several approaches have been made for studying the static and dynamic response of such structures. Essentially, these approaches are based on two-dimensional classical and shear deformation theories or three-dimensional elasticity theory. There are not many solutions for laminated circular cylindrical shells based on three-dimensional elasticity because of considerable mathematical difficulties involved in solving governing differential equations for general boundary and loading conditions. However, the three-dimensional elasticity solutions for simpler loading and boundary conditions would be useful since these could be used to verify the approximations and limitations of the two-dimensional, classical and shear deformation theories. Recently, Noor and Burton[1] have reviewed fairly exhaustively the available analytical and numerical solutions for laminated shells.

2. Present analysis

A detailed investigation on the static response of simply supported transversely isotropic cylindrical shell of revolution[2] and shell panel[3] has been made using three-dimensional elasticity approach The three-dimensional equilibrium equations, in terms of displacements, can be obtained using the stress–strain and strain–displacement relations. These equations form a set of three second-order partial differential equations with variable coefficients, in terms of radial coordinate. The solution of these equations is taken in terms of Fourier infinite integral or Fourier series in the longitudinal direction, depending on whether the shell is of finite or infinite length, and in terms of Fourier series in the circumferential direction to account for the symmetry of the load or boundary conditions. This results in a set of three ordinary differential equations in terms of radial coordinate. The exact solution of these equations is mathematically tedious. However, the exact solutions for the transversely isotropic or unidirectional laminated shell of revolution and shell panel, subjected to asymmetric loads, have been obtained using displacement function approach. Using this approach the solution can be obtained in the form of Bessel functions. These functions do not pose any convergence difficulties as they exhibit orthogonal property. However, this method is applicable only to transversely isotropic and unidirectional, laminated shells, with the longitudinal axis being the isotropic plane. If the plane of isotropy changes from longitudinal axis to circumferential axis, the displacement functions, defined earlier, do not result in Bessel's equations Hence, the displacement function approach cannot be extended to the most commonly used cross-ply laminates. To overcome this difficulty an approximate solution has been developed by reducing the ordinary differential equations with variable coefficients to those with constant coefficients, by making the

assumption that the ratio of shell thickness to mean radius is small when compared with unity, and hence, can be neglected. The approximate solution has been developed for a simply supported, single layered, orthotropic and cross-ply laminated shell panel and cylindrical shell of revolution, subjected to asymmetric[4], as well as axisymmetric[5] loads. The exact and approximate solutions have been extended to the study of free vibration problem of simply supported, cylindrical shell of revolution. A detailed study has been made to establish the limitation of this approximate solution by comparing the results with the exact solution.

For a laminate with a large number of layers, both exact and approximate solutions, result in a large system of algebraic equations for each pair of Fourier harmonics in longitudinal and circumferential direction. In order to reduce the number of simultaneous equations to be solved, to a minimum, these solutions are reformulated using a transfer matrix approach and has been demonstrated with the help of a few examples.

Solutions based on classical, first order, and higher order shear deformation theories have been obtained, and detailed comparison of these results with the results of exact and approximate solutions have been made for several thickness to radius ratios, and material properties and types of loads.

3. Conclusions

From the detailed numerical comparisons provided in the thesis the following conclusions can be arrived at

3.1. *Static response*

(a) *Transversely isotropic shell*

The results obtained using classical and first-order shear deformation theories show good agreement with those obtained from elasticity solution for shell thickness to mean radius ration (H/R) less than 0.1, and modulus ratios (E_r/E_θ) less than 11.52. The higher order shear deformation theory predicts different stresses and displacements closer to elasticity results even for thick shell ($H/R = 0.2$), but for modulus ratio (E_θ/E_θ) less than 11.52.

The variation of longitudinal and circumferential stresses over thickness exhibit nonlinearity for shell thickness ratios (H/R) greater than or equal to 0.2. Further, the nonlinearity is more pronounced for modulus ratios greater than 11.52. All the shell theories, considered in the present investigation, fail to predict accurate results for circumferential stress. The transverse shear stress shows parabolic variation over thickness for single-layered shell. The magnitude of the radial stress is very small when compared to the longitudinal and circumferential stresses.

The variation of radial displacement is almost constant for shell thickness ratio up to 0.1 For thick shell ($H/R = 0.2$) this displacement shows nonlinear variation over thickness. The classical shell theory underpredicts to the extent of 14%, even for thin shell ($H/R = 0.05$). For the thickness to mean radius ratio (H/R) equal to 0.2 the percentage error can be as large as 66% with respect to elasticity results. The first order and higher order theories predict this displacement reasonably well. The results deviate less than ±10% from elasticity results.

(b) *Laminated shell*

The approximate method, developed to solve the orthotropic shell, predicts accurate results for the shell thickness to mean radius ratios up to 0.2. In most of the practical applications, the lamina thickness-to-mean radius ratio is less than 0.2. Hence, this method can be extended to laminated shells.

The longitudinal and circumferential stresses in the laminated shell exhibit nonlinear variation for thickness ratios $H/R = 0.2$, for all the modulus ratios considered, and for thickness ratio $H/R = 0.1$ for modulus ratio (E_θ/E_θ) greater than 11.52. The circumferential stress predicted by shell theories show a considerable deviation from the elasticity results, especially on the inner surface of the shell.

The variation of transerverse shear stress over thickness is not parabolic for $H/R = 0.2$ and for modulus ratio greater than 11.52. The maximum shear stress predicted by shear deformation theories is reasonably closer to that obtained by elasticity solution, except for the position at which the maximum shear stress occurs. The maximum shear stress along the longitudinal direction occurs at $x = 0.3$ L for the patch load considered in this investigation.

The radial displacement is almost constant over thickness for $H/R = 0.1$ and nonlinear for $H/R = 0.2$. The maximum value occurs at the loaded surface of the shell. The classical shell always underpredicts this displacement, whereas shear deformation theories predict this displacement within ± 10% accuracy.

3.2. *Dynamic response*

Using the exact and approximate method of solutions the results have been obtained for single and unidirectional laminated circular cylindrical shell of revolution for the thickness ratio $H/R = 0.1$. The fundamental frequencies have been tabulated for the first few Fourier harmonics. The results obtained using approximate solution have shown good agreement with the exact solution results.

For both exact and approximate solutions it is difficult to formulate the polynomial equation. In the exact solution the frequency term is embedded in the argument of Bessel function. Hence, a trial and error method has been followed. For this, first a starting value for the frequency is assumed. Then, by adjusting the frequency by a suitable amount, the determinant value has to be calculated until the sign of the determinant, for two successive values of frequency, is different. Finally, by linear interpolation the magnitude of the frequency, for which the determinant is zero, can be evaluated.

The elastic solutions, result in a large system of algebraic equations. With the increase in the number of laminae in the laminate, the size of these equations also increases. In order to reduce the number of simultaneous equations to be solved, to a minimum, these solutions are formulated using a transfer matrix approach. This approach has been demonstrated with the help of a few examples.

References

1. NOOR, A. K. AND BURTON, W. S. — Assessment of compuatational models for multilayered composite shells, *Appl. Mech. Rev.*, 1990, **43**, 76–96.
2. CHANDRASHEKARA, K. AND KUMAR, B. S. — Analysis of a thick transversely isotropic circular cylindrical shell subjected to asymmetric load, *Acta Mech.*, 1990, **84**, 63–75.
3. CHANDRASHEKARA, K. AND KUMAR, B. S. — Analysis of a thick orthotropic cylindrical shell, *Mech. Res. Commun.*, 1992, **18**, 395–401.
4. CHANDRASHEKARA, K. AND KUMAR, B. S. — Static analysis of a thick laminated circular cylindrical shell, *J. Pressure Vessel Technol.*, ASME, 1993, **115**, 193–200.
5. CHANDRASHEKARA, K. AND KUMAR, B. S. — Static analysis of a thick laminated cylindrical shell subjected to axisymmetric load, *Composite Struct.*, 1993, **23**, 1–9.

Thesis Abstract (Ph.D.)

General and sensitivity analysis of water distribution networks by Rayapeddi S. N. Datta

Research supervisor: K. Sridharan
Department: Civil Engineering

1. Introduction

Analysis forms a core area of studies in water distribution systems, whether for prediction of the performance of an existing system or for the design of a new system. Simulation studies on existing systems require estimation of network parameters, such as Hazen–Williams coefficients, wherein also analysis plays an important role, whether the parameters are estimated by direct calibration or optimization techniques. The present study deals with the general analysis and parameter estimation problem using weighted least squares method based

on sensitivity analysis technique, in water distribution systems[1]. The general analysis problem is defined as network analysis in which the unknowns comprise a mix of nodal heads, nodal consumptions and pipe resistances; the unknown pipe resistances may be related to each other for a group of pipes.

2. Formulation

Three types of formulations, namely, the nodal, the path and the node and path formulations are presented for the general analysis problem in water distribution networks. Four methods are presented for the solution of the general analysis problem in water distribution networks. Four methods are presented for the solution of the general analysis problem: Node–Picard (N–P) method–nodal formulation solved by Picard method, Node–Newton (N–N) method–nodal formulation solved by Newton method, Path–Newton (P–N) method–path formulation solved by Newton method and Node Path–Picard (NP–P) method–node and path formulation solved by Picard method. The N–P and NP–P methods are extensions to the general analysis problem of the well-known linear theory for network analysis, which has been developed for the classical analysis problem wherein the nodal heads and pipe flows are solved assuming the pipe resistances are known. The P–N method is a more generalized approach of the path formulation than available in the literature. Guidelines are presented to check the wellposedness of a general analysis problem.

3. Comparative study of general analysis methods

A comparative study of the four methods is made covering different aspects such as the number of equations, size and density of matrix, accuracy of solution, robustness to initial estimates and convergence characteristics using problems of varied complexities. The self-starting N–P method is found to be very robust to the initial estimates. However, the method shows convergence problems in the form of unduly large numerical fluctuations when pipes with extremely low resistance associated with head loss of less than 1 mm are present in the network. Even in such cases, the solution is found to be poor only in the vicimty of these pipes, whereas the solution away from these pipes is good. A node-merging technique, which yields good results in such cases, is proposed. The N–N method is found to converge only when the initial estimates are reasonable and the convergence behaviour is similar to that of N–P method. The P–N method is found to be the fastest in convergence and yields solution with the smallest residues among all the four methods. The behaviour of the method is equally good in the presence of extremely low as well as extremely high resistance pipes. Though the method is more robust compared to the N–N method, the initial flow estimates should satisfy the node found to give convergence to all problems with a relaxation parameter of 0.5. However, in the presence of very high resistance pipes, the method may show accuracy problems. The initial flow estimates for the NP–P method need not satisfy the node continuity equations unlike in the case of P–N method.

4. Applications of general analysis algorithm

The usefulness of the general analysis algorithm as a tool for direct calibration of network models is demonstrated for the principal transmission mains network system of Bangalore city. The network handles a total supply of 4.837 m^3/s (92 mgd) from three sources, and includes 15 ground-level reservoirs, 8 overhead tanks, 7 pumps, with the pipes varying in size from 250 to 1750 mm. Two operating conditions with different demand patterns are used for model calibration.

The usefulness of the general analysis algorithm in dealing with problems of system operation is demonstrated for the above network. Three different operating conditions are studied, namely, normal supply condition, starved supply condition and augmented supply condition. For these conditions, operating policies in terms of identification of valve settings are determined for satisfying the specified demand patterns. The utility of the general algorithm in planning system modifications is also demonstrated by designing a pump and the associated 4.8-km long pipeline between two specified nodes in the existing network.

5. Parameter estimation

The weighted least squares (WLS) method using sensitivity analysis technique is proposed for the estimation of parameters in water distribution systems. The parameters considered are the Hazen–Williams coefficients for the pipes. The objective function used is the sum of the weighted squares of the differences between the computed and the observed values of the variables. The WLS method can elegantly handle multiple loading conditions with mixed type of measurements such as heads and consumptions, different sets and number of

measurements for each loading condition, and modifications in the network configuration due to inclusion or exclusion of some pipes effected by valve operations in each loading condition. Effects of choice of weights and imposition of constraints on the relative changes of parameters at any literation are discussed.

The WLS method is applied for estimating the pipe roughness parameters for the Bangalore city network. Three operating conditions with different network configurations, different valve settings, different types of observations, and different number of observations are considered. The method is applied for single as well as multiple loading conditions.

References

1. SHAMIR, U. AND HOWARD, C D. D. — Water distribution systems analysis, *J. Hydraul. Div., ASCE*, 1968, **94**, 219–234.
2. BOULOS, P. F. AND WOOD, D. J. — Explicit calculation of pipe network parameters, *J. Hydraul Engng, ASCE*, 1990, **116**, 1329–1344.
3. LANSEY, K. E. AND BASNET, C. — Parameter estimation for water distribution networks, *J. Wat. Resource Plann. Mgmt, ASCE*, 1991, **117**, 126–144.

Thesis Abstract (M.Sc. (Engng))

Some studies on helicopter trim and stability by S. N. Omkar

Research supervisor: J. Nagabhushanam
Department: Aerospace Engineering

1. Introduction

In general, trim and stability constitute two of the most important aspects of the design and development of any rotary wing aircraft. Trim concerns the evaluation of the equilibrium state of the aircraft under the combined action of aerodynamic, inertial and gravitational forces and moments for a given flight condition while stability refers to its tendency to return to the equilibrium state following a disturbance.

The stability and performance of the helicopter are strongly influenced by its trim state due to the inherent coupling of the rotor forces with the forces acting on the fuselage and other control surfaces. With increasing demand for highly manoeuverable helicopters with extended flight regimes, many modern helicopters are found to be more susceptible to instabilities. This necessitates the use of stability and control augmentation systems whose dependence could be reduced by proper understanding of the dynamical behaviour of the helicopter.

Analysis of dynamic stability of a helicopter rotor is a complex phenomenon involving nonlinear couplings of aerodynamic, inertial and elastic forces. For stability investigations the trim parameters for a given flight condition are computed first and later the governing equations of the system are perturbed about the computed trim to obtain perturbed linear equations. These equations are analyzed by Floquet method to assess the stability of the system.

Most of the trim and dynamic stability analysis has been carried out for rotor in isolation[1]. Some researchers have studied the stability aspects by including the fuselage[2]. Though complete helicopter representation has been considered for trim analysis[3], very little literature exists on the stability investigations with full helicopter configuration. Hence, work has been carried out to study the stability of the rotor by considering the complete helicoter configuration.

2. Analytical model

The rotor is modelled as multiblade with rigid flap and lead–lag motions about a coincident offset hinge and hinge restraint springs. The rotor shaft can have a tilt. The blade can have root cutout and geometric linear

twist distribution. The main and tail rotor inflows are evaluated using the momentum theory. The effect of unsteady aerodynamics is represented in the form of dynamic inflow. Dynamic inflow essentially is the representation of variation of inflow with respect to time, radius and azimuth in the form of state aerodynamic force and moment characteristics. The aerodynamic forces of vertical tail and horizontal tail are based on their geometry and aerodynamic parameters.

3. Derivation of equations and their solutions

The equations of motion are derived from Lagrangian approach. For trim analysis a system of 21 nonlinear algebraic equations are developed and solved simultaneously using Newton–Raphson iterative technique. As the differential equations for the rotor contain periodic terms, the stability analysis is carried out first by determining the Floquet's transition matrix and then by solving it as an eigenvalue problem.

The algebraic manipulations involved in derivation or governing equations are extremely tedious and manual derivation is error prone. Hence, governing equations are derived by using a special-purpose symbolic processor DEHIM-II (dynamic equations of helicopter interpretive model–version II).

Efficient computational schemes in terms of handling the lengthy nonlinear symbolic governing equations are developed which makes their handling simpler and easier. A preprocessor is developed to code the symbolic equations and prepare a data file. This data file is in turn interlinked with numerical analysis programs. The data files of the equations themselves are used to compute the derivatives of the equations with simple manipulation of the data. This scheme helps to totally avoid the preparation of FORTRAN statements of the symoblic equations and their derivatives with respect to governing variables. The computational scheme adopted for this work are totally new from that of any previous investigations.

4. Results

Parametric studies are carried out to understand the influence of the following modeling parameters on trim and stability analysis: i) Hinge offset, ii) Shaft tilt, iii) c.g., location, iv) lag dynamics, v) lag frequency, and vi) main rotor blade twist.

The study of inclusion of hinge offset indicates that it can bring considerable changes in the control pitch settings, blade response, fuselage attitudes, lag mode damping and the roll and pitch mode dampings.

The study of shaft tilt effects indicates that the cyclic pitch and cyclic flap angles and fuselage attitudes are quite sensitive to shaft tilt. It is also observed that the lag damping and pitch mode damping are significantly influenced at forward flight. A similar observation can be made from studies on the effect of c.g., location.

The study of inclusion of lag dynamics on trim shows that the influence of inplane motion on trim is not very significant. The influence of considering lag trim for stability shows a marginal influence on lag mode damping at high forward speeds. The variation of lag frequency has significant influence on trim and stability analysis. Studies carried out on soft and stiff inplane rotors also emphasize this fact.

The studies on the influence of blade twist show some marginal influence on trim and stability values.

The effects of wake dynamics are accounted for by considering a dynamic inflow model. It is seen from the various parametric studies that the aerodynamic modelling has a very significant influence on the stability values and hence aerodynamic modelling becomes a major factor in accurately predicting the stability values.

5. Conclusions

The present work gives a comprehensive model for trim and stability analysis of the helicopter. The work indicates the importance of various parameters and also gives a direction for the type of parameters and the range of values for each parameter that need to be considered for parametric studies during the design phase of the helicopter. The work has resulted in an integrated software which for a given helicopter data calculates the trim parameters and from that the stability values. This approach, method and software will be useful for industrial application where one has to consider the effect of various parameters on trim and stability.

References

1. PETERS, D. A. — Flap–lag stability of helicopter rotor blades in forward flight, *J. Am. Helicopter Soc.*, 1975, **20**, 2–13.

2. NAGABHUSHANAM, J. AND GAONKAR, G. H. — Rotorcraft air resonance in forward flight with various dynamic inflow models and aeroelastic couplings, *Ninth European Rotorcraft Forum*, Sept 13–15, 1983, Stresa, Italy, p. 52.

3. PAVAN KUMAR, R. S V. S. — *General helicopter trim with improved rotor modelling*, M. S. Thesis, Indian Institute of Science, Bangalore, December 1988.

Thesis Abstract (M.Sc. (Engng))

Studies on oil flotation of wolframite by T. V. Vijaya Kumar

Research supervisors: U. B. Nayak and R. M. Mallya
Department: Metallurgy

1. Introduction

All tungsten minerals are friable and the conventional concentrating processes are hindered by the production of excessive fines or slimes resulting in low grades and recoveries. The processing of such fine particles by alternative routes is becoming increasingly important for the selective recovery of fine particles or for the treatment of ores containing slimes. Oil flotation is a potential technique which involves the addition of an oil, immiscible in water, in varying amounts to the mineral pulp. This technique based on stabilization of emulsions by fine particles has several advantages over the conventional froth flotation in recovering fine mineral particles[1].

This work deals with the selection of an oil for this purpose on which fundamental work has been carried out. The studies include the effect of important process parameters such as pH, collector concentration, amount of immiscible organic phase, size of the particles, etc., on oil flotation of wolframite with a view to optimize them. Studies were also carried out to find the effect of cations such as Fe(II), Mn(II), Ca(II) and Fe(III) that are usually present in wolframite pulps on oil flotation of wolframite.

2. Materials and experimental methods

High-grade purified wolframite ore (70% WO_3) and quartz (99.5% SiO_2) were used. Technical-grade sodium oleate of BDH make was used as collector. *n*-Pentane, *n*-hexane, *n*-heptane, benzene, cyclohexane, isobutyl alcohol of 99% minimum purity and commercial-grade kerosene were used as organic liquids in oil flotation experiments.

Oil flotation experiments were performed in a 125-cc-capacity separatory funnel. Wolframite ore sample of 3.0 is conditioned in 100 cc of aqueous collector solution to which 10 cc of organic liquid is added. This mixture is agitated vigorously after which wolframite is floated into the emulsion or oil phase. The interfacial tensions between aqueous collector solutions and different organic liquids were determined at room temperature by means of Traube stalagmometer by drop number method. The zeta potential studies were conducted using 'Zeta–Meter system 3.0', a commercially available electrophoresis apparatus.

3. Results and discussion

Preliminary oil flotation experiments conducted on wolframite under identical experimental conditions using different oils indicated that *n*-pentane, *n*-heptane and kerosene which are characterized by straight chain structure responded well with recoveries of 63.84, 60.23, 58.79 and 58.49%, respectively. On the other hand,

benzene and cyclohexane that are characterized by cyclic structure responded poorly with recoveries of 15 62 and 36.59%, respectively. Interfacial tension measurements between different oils and aqueous collector solutions show that lowering of interfacial tension is not the property *per se* which is the stabilizing factor contributing to the stability of oil droplet dispersion in solution. *n*-Pentane was chose as oil for subsequent detailed investigations because of its effectiveness in recovering the wolframite particles.

Optimization of process parameters was carried out varying one parameter at a time, and keeping the values of the remaining parameters constant. The conditions optimized for almost 100% of 10 mg/l and 23% *n*-pentane by volume of total liquid content. The maximum recovery obtained at pH 7.0 could be attributed to the more surface activity of inomolecular complex species $HO1_2$ than either $O1^-$ or HO1 on wolframite particles[2]. Zeta potential studies on the charge characteristics of wolframite indicate that the mode of adsorption of sodium oleate on wolframite was due to chemisorption. It was found that finer the size of the particles, better was the recovery which shows the efficiency of this process in recovering finer particles.

Ca(II) and Mn(II) showed an activating effect on oil flotation of wolframite with a maximum recovery of about 97% in the pH range of 4.0–11.0. Fe(II) has an activating effect in the acid pH range followed by a depressing effect in alkaline pH range. Fe(III) has profound antagonistic effect on oil flotation of wolframite in the pH range 4.0–11.0. These results were explained by zeta potential measurements carried out under similar conditions and hydrolysis of metal cations under various pH conditions[3].

Quartz was found to be nonfloatable under the optimized conditions for oil flotation of wolframite. The separation of wolframite from its major gangue, quartz, was established by means of artificial mixtures of these two minerals of different weight proportions under the optimized conditions with over 90% wolframite reporting to oil/emulsion phase. Satisfactory results have been obtained using kerosene in place of *n*-pentane under the same experimental conditions which could be a possible alternative to *n*-pentane because of its low cost.

4. Conclusions

The conclusions drawn from the investigations are as follows:

1. The structure of oil molecules has a significant bearing on the judicious selection of oil phase. Short, straight chain structured oils responded better as compared to cyclic structured oils in the oil flotation of wolframite. *n*-Pentane was found the most suitable among the tested oils in a homologous series.

2. Optimum conditions for oil flotation of wolframite were pH 7.0 at a sodium oleate concentration of 10 mg/l and 23% *n*-pentane by volume of total liquid content. A recovery of 99 57% was recorded for –400 # (BSS) size particles of wolframite.

3. The negatively charged wolframite particles in the presence of metal cations and sodium oleate have a beneficial effect in contrast to the positively charged wolframite particles under the same conditions that proved to be detrimental.

4. Use of kerosene in place of *n*-pentane on an artificial mixture (1:1) of wolframite and quartz gave encouraging results with 92.38% of wolframite reporting to oil/emulsion phase and is recommended as oil phase due to its low cost compared to other organic liquids used.

References

1. STRATTON–CRAWLEY, R. *Oil flotation: Two liquid flotation techniques, Beneficiation of mineral fines–Problems and research needs,* (Somasundaran, P. and Arbiter, N., eds), 1979, pp.317-330, AIME, USA.

2. ANANTHAPADMANABHAN, K. P. AND SOMASUNDARAN, P. *J. Colloid Interface Sci.*, 1988, **22**, 104–109.

3. MARINAKIS, K. I. AND KELSALL, G. H. Effect of lattice cations, silicate ions and fluorosilicate ions on two-liquid flotation of tungsten minerals, *Trans. IMM* (Lond.), 1987, **96**, C63–C68.

Thesis Abstract (Ph.D.)

Study of amorphous phase formation by mechanical alloying in Ti based systems by B. S. Murty

Research supervisors: S. Ranganathan and M. Mohan Rao
Department: Metallurgy

1. Introduction

Mechanical alloying (MA) has emerged in recent years as a viable alternative route to rapid solidification processing (RSP) for the synthesis of nanocrystals, metastable crystalline, quasicrystalline and amorphous phases[1]. In MA, pure metal powder mixture is milled in high-energy ball mills to achieve alloying at the atomic level.

The present study was focused mainly on the formation of amorphous phase in Ti-based binary and ternary alloys by MA. The study involved the synthesis and characterization of the amorphous phases using X-ray diffraction, transmission and scanning electron microscopy. The thermal stability of these phases was studied using a differential scanning calorimeter. The thermodynamics of glass formation has been worked out for the binary and ternary systems of interest to establish the theoretical glass-forming ranges (GFRs).

2. Experimental details

MA has been carried out in a Fritsch planetary mill and a Spex vibratory mill using WC vial and WC balls. Various milling parameters such as milling intensity (speed), ball-to-powder weight ratio, number of balls, wet (toluene) and dry (argon) milling have been studied (Table I). Three compositions in the Ti–Ni–Cu system corresponding $Ti_{50}Ni_{50-x}Cu_x$ ($x \approx 10, 25, 40$) have been melt spun at 40 ms^{-1} for comparison.

3. Results and discussion

At the milling intensity of 6 (490 rpm) a GFR of 10–70 at.% Ni and 10–50 at.% Cu was observed for Ti–Ni and Ti–Cu systems, respectively, after 20 h of wet milling. The GFR obtained by MA in the Ti–Ni system in the present study is much wider than that reported earlier by RSP (23–46 and 55–64 at.% Ni)[2] and by MA (28–72 at.% Ni)[3]. However, in the case of Ti–Cu the earlier reports have given a wider GFR[4]. These differences are attributed to different milling conditions. Enthalpy calculations based on Miedema's model have shown a small negative enthalpy of mixing for the amorphous phase in Ti–Cu system (–3 kJ at 50 at.% Cu) which explains the narrow GFR in Ti–Cu system.

Increase in the milling intensity to 8 (600 rpm) has narrowed down the GFR in Ti–Ni system to 10–40 at.% Ni and widened it in Ti–Cu system to 10–60 at.% Cu. This was found to be due to the severe contamination by WC in the case of Ti–Ni samples which was found to prevent the alloy formation and in turn the amorphous phase formation. No contamination was observed in Ti–Cu samples.

Table I

System	Composition
$Ti_{100-x}Ni_x$	$x = 10, 20, 30, 40, 50, 60, 70, 80, 90$
$Ti_{100-x}Cu_x$	$x = 10, 20, 30, 40, 50, 60, 70, 80, 90$
$Ti_{40}Ni_{60-x}Cu_x$	$x = 10, 20, 30, 40, 50$
$Ti_{50}Ni_{50-x}Cu_x$	$x = 10, 15, 20, 25, 30, 35, 40$
$Ti_{60}Ni_{40-x}Cu_x$	$x = 10, 20, 30$
$Ti_{100-x}Al_x$	$x = 10, 20, 30, 40, 50, 60, 70, 80, 90$

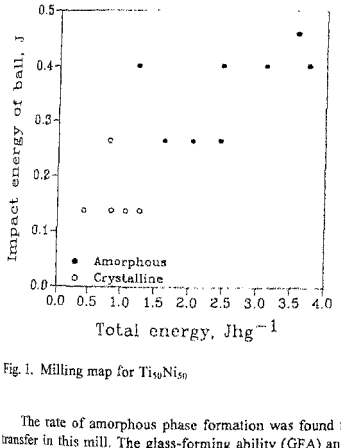

Fig. 1. Milling map for $Ti_{50}Ni_{50}$

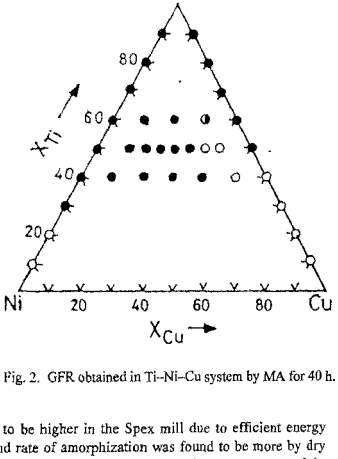

Fig. 2. GFR obtained in Ti–Ni–Cu system by MA for 40 h.

The rate of amorphous phase formation was found to be higher in the Spex mill due to efficient energy transfer in this mill. The glass-forming ability (GFA) and rate of amorphization was found to be more by dry milling. The study of $Ti_{50}Ni_{50}$ samples at different milling intensities with different ball-to-powder weight ratios and varying the number of balls has shown that all the milling parameters can be related to two energy parameters, namely, the impact energy of the ball and the total energy. A milling map was constructed with these energy parameters to separate out the glass formation regime. Figure 1 shows the milling map for $Ti_{50}Ni_{50}$ which indicates that a minimum energy of ball of *0.15 J* and a total *milling energy of 1.5 J h g*$^{-1}$ is essential for amorphous phase formation for this composition. These milling maps can be treated as glass-forming maps as they define conditions for glass formation by MA.

The GFR in the Ti–Ni–Cu system was found to be $x = 10$–20 for $Ti_{60}Ni_{40-x}Cu_x$, $x = 10$–30 for $Ti_{50}Ni_{50-x}Cu_x$ and $x = 10$–40 for $Ti_{40}Ni_{60-x}Cu_x$ after 40 h of MA (Fig. 2). The Cu-rich compositions were found to be difficult to amorphize by MA. The extension of the Miedema's model to ternary alloy system has yielded a GFR which compares fairly well with that obtained by MA in this system (*Fig. 3*). *The rate of amorphization* and thermal stability was found to be maximum for the middle composition in each of the three groups.

The study of $Ti_{50}Ni_{50-x}Cu_x$ ($x = 10$, 25, 40) by melt spinning has shown that the GFA is more for Cu-rich composition in contrast to that observed by MA. This was found to be due to the lower *liquidus* temperature for the Cu-rich composition when compared to Ni-rich compositions which enhanced the glass-forming ability of Cu-rich compositions. This clearly brings out the difference in the factors controlling glass formation by *RSP* and *MA*. In the case of RSP, the ability to undercool *the liquid below glass transition* temperature is important and thus the liquidus temperature of the alloy is the major factor controlling glass-forming ability. In contrast, in the case of MA, the availability of driving force for the amorphous phase and the anomalous diffusion of *one element in the other plays a key role in* deciding the glass-forming ability.

Glass formation by RSP is very difficult in the case of systems containing a cascade of peritectics in their phase diagrams. Ti–Al is such a system, in which glass formation has not been reported so far by RSP. In the present study by MA *this system has shown a very wide* GFR of 10–60 at.% Al at the milling intensity of 6 and still wider (10–75 at.% Al) at the milling intensity of 9 (645 rpm). The GFR predicted from the thermodynamic calculations compares fairly well with the above result. The amorphization was found to start when the strain in Ti reached a critical value.

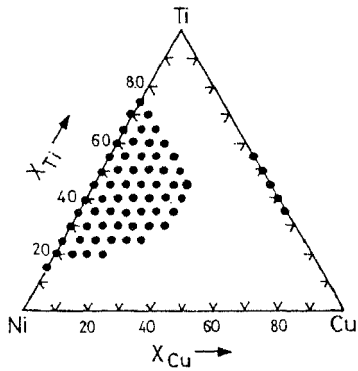

Fig. 3. GFR calculated for Ti–Ni–Cu system using Miedema's model.

4. Conclusions

1. The GFR in Ti–Ni, Ti–Cu, Ti–Ni–Cu and Ti–Al systems has been established by MA.
2. All the milling parameters have been reduced to energy parameters and in a two-dimensional plot of these energy parameters (milling maps) the glass formation regime has been isolated.
3. The factors controlling the GFA by RSP and MA were identified.
4. The simplistic Miedema's model was shown to predict the GFR fairly well in the systems studied.

References

1. ARZT, E. AND SCHULTZ, L. (eds) *New materials by mechanical alloying techniques*, 1989, Verlag.
2. BUSCHOW, K. H. J. *J. Appl. Phys.*, 1984, **56**, 304–306.
3. SCWARTZ, R. B., PETRICH, R. R. AND SAW, C. K. *J. Non-Cryst. Sol.*, 1985, **76**, 281–302.
4. POLITIS, C. AND JOHNSON, W. L. *J. Appl. Phys.*, 1986, **60**, 1147–1151.

Thesis Abstract (Ph.D.)

Manufacturability analysis of cast components by B. Ravi

Research supervisor: M. N. Srinivasan
Department: Mechanical Engineering

1. Introduction

The design of a casting influences its manufacture, reflected in its quality, productivity and cost. Analysis of various geometric, material and process factors influencing manufacturability enables the designer to foresee potential problems, and incorporate modifications to overcome drawbacks before freezing the design.

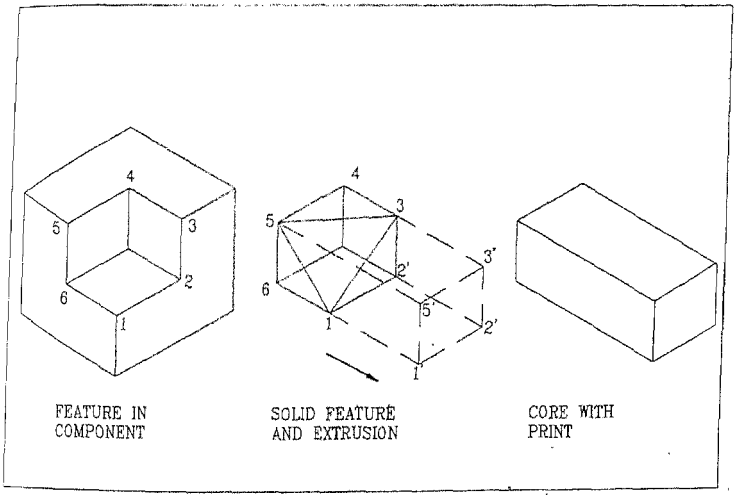

Fig. 1. Core print design.

Heuristics[1] employed by practising engineers are applicable to a specific class of parts and do not provide any quantitative measure for comparing various alternatives. Computer-aided simulation of molten metal flow[2] and solidification[3] requires a reliable database of metal and mould properties, and are computation intensive. Moreover, the mould geometry for simulation is obtained by interactively modifying the component geometry[4] which is itself a time-consuming task and requires experience.

In this work, an objective, automatic and rapid approach to the assessment of manufacturability of castings has been taken up by recognizing important geometric features from the solid model of the casting and analyzing them by a set of criteria developed for the purpose.

2. Casting features

Casting features have been classified as solids, interfaces, and parting contours. Parting line, the contour along which casting-cope, casting-drag and cope-drag interfaces meet, has been generated by projecting the boundary of the part sihouette back to the component. The interface of the casting with each mould segment is then generated to obtain the cope and drag portions of the pattern.

Depression features have been recognized from the solid model of the component based on the boundary loops separating the feature faces from the rest of the solid. Undercut regions are recognized using the direction of face normals with respect to the draw direction. Solids corresponding to the depression features which require coring are extracted and extruded to obtain the core prints (Fig. 1).

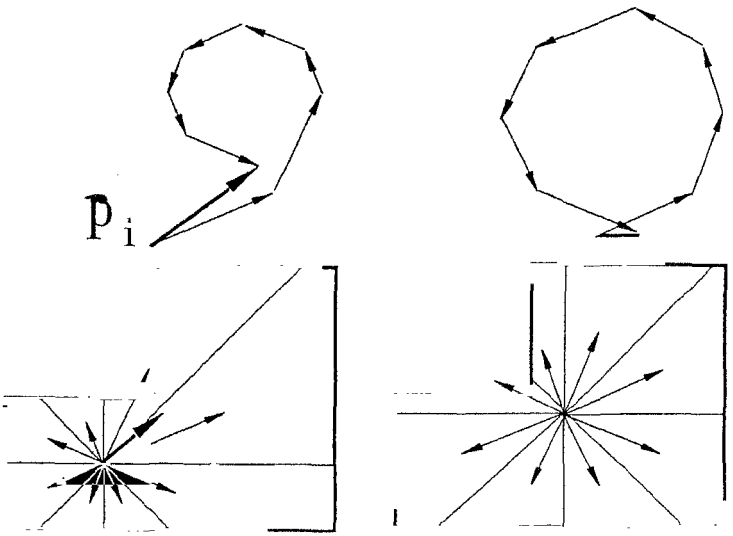

Fig. 2. Hot spot location by flux vector technique.

The location of the gating system has been generated along the parting. Molten metal rising in the mould is then simulated by considering the instantaneous flow rate of metal and cross-section area of the casting. This gives the filling time of the mould. If it is different from the recommended pouring time, then the gating entities are redesigned.

A novel geometry-driven thermal analysis program for identifying hot spots and tracing feed metal flow paths in a casting has been developed for locating the feeders (Fig. 2). The casting is divided into a number of pyramidal regions from a point $\bar{p}_i$ inside the casting, and flux vector h_{ij} computed for each. The resultant $\bar{H}_i$ of these gives the direction and magnitude of the largest thermal gradient. By proceeding along this vector, the nearest hot spot is reached. The influence of gating, coring, feed aids (chills, insulation, etc.) and pouring parameters has been considered in the computation. Modulus of the region around the hot spot has been automatically computed for feeder dimensioning. The equations are given below.

Let ΔV_{ij} be the volume of the jth pyramid (or sector in 2D), ΔA_{ij}, the surface area of its base, β, solid angle subtended by the base of the pyramid at its apex, and $\bar{r}_j$, the position vector of the centroid of pyramid base. Then

$$\text{Flux vector } \bar{h}_{ij} = \frac{3\beta}{2\pi} \frac{\Delta V_{ij}}{\Delta A_{ij}} \frac{(\bar{p}_i - \bar{r}_j)}{|\bar{p}_i - \bar{r}_j|}$$

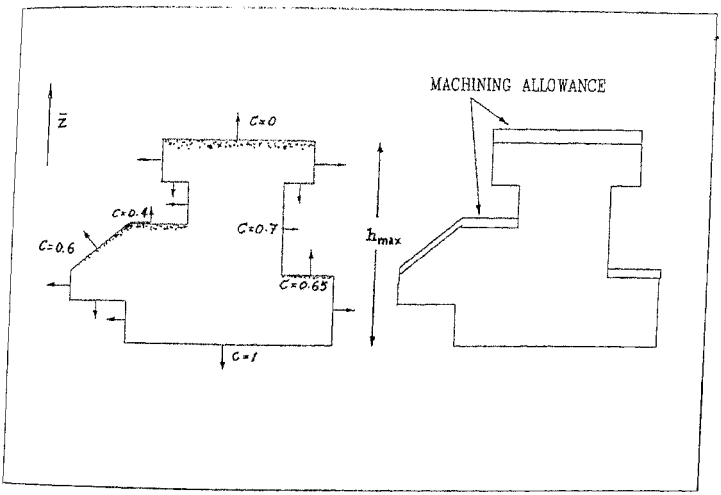

Fig. 3. Influence of location and orientation on surface quality.

$$\text{Resultant } \bar{H}_i = \sum_j \bar{h}_{ij}$$

$$\text{Temperature } T_i = \frac{1}{n} \sum_j |\bar{h}_{ij}|$$

$$\text{Modulus } M_i = \frac{\sum_j \Delta V_{ij}}{\sum_j \Delta A_{ij}}$$

$$\text{At the hot spot, } |\bar{H}|/T < \varepsilon$$

where ε is a limiting value tending to zero.

3. Design criteria

Criteria for the quantitative assessment of the manufacturability of a casting have been developed after a scientific analysis of the heuristics employed in design protocols. Each criterion has been written in terms of geometric parameters of a particular feature and its relation with other entities in the casting. The value returned by the criterion indicates the manufacturability for the considered aspect. From among 31 criteria developed in this work, a few typical ones are discussed here.

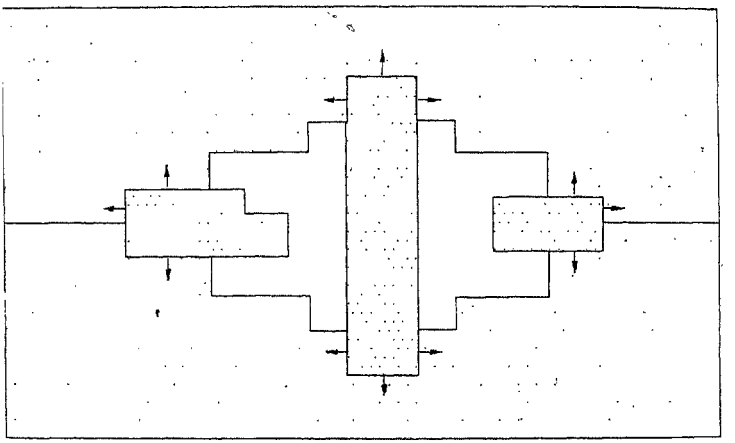

Fig. 4. Assessment of venting based on the direction of normals to print faces.

The choice of parting was assessed for flatness, undercut, draw, draft, surface quality, flash, dimensional stability and envelope volume. Undercut criterion computes the volume of undercut given by the product of the projected area of an undercut face f_i and its distance H to the parting P or the nearest face in between (Fig. 3).

$$C_{\text{undercut}_i} = A_s(f_i)\,(\overline{n}_i \cdot \overline{d}_i)\,H(f_i, \mathrm{P}).$$

Cores were analysed using criteria for shape, size, modulus, aspect ratio, support, coring volume and venting. For arriving at the venting criterion, the area of core in contact with the metal, which leads to gas generation, was compared with the core print area available for dissipating the same (Fig. 4).

$$C_{\text{venting}_i} = \frac{\sum_j 0.5(2 + \overline{n}_j \cdot \overline{z}) A_s(f_j \in \mathrm{F}_i^M)}{\sum_j A_s(f_j \in \mathrm{F}_i^C)}.$$

For the flow of molten metal, sections in the component have been evaluated for thickness, uniformity of size and change in angle. Height of free fall D from the ingate G_i to the point of impingement p_k and the angle of impingement (Fig. 5) are determined.

$$C_{\text{impinge}_i} = 0.5(1 + (\overline{n}_i \cdot \overline{n}_k))D(G_i, p_k) / d_{\max}.$$

Other criteria for gating include coverage, flow distance, ease of fettling and yield. Feeding efficiency, location of shrinkage cavities, temperature, temperature gradient, ease of fettling and casting yield were assessed for feeder design. A visual representation for the comparison of the assessed values of various alternatives has been developed.

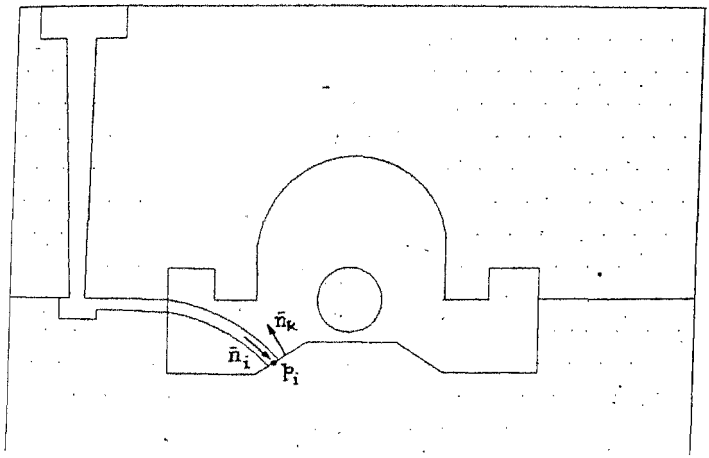

Fig. 5. Impingement of melt jet from ingate on to mould wall.

4. Implementation and results

The programs developed for parting, coring, gating and feeding have been integrated in a computer-aided simultaneous engineering system (Fig. 4) for product analysis and design of mould assembly–PADMA. The 3D geometric data of the casting model was accessed by each program for recognizing various features and assessing its manufacturability. The system has been linked to solid modellers like AutoCad (release 11) through a standard data exchange format. A few typical engineering components such as bearing support, lug and valve have been analyzed by this system.

The program was validated by experimentation on selected casting of Al 12% eutectic alloy poured in green sand moulds. The location of shrinkage cavities were the same as the computed hot spots.

5. Conclusions

This investigation has enabled delineation of the rationale underlying a number of design guidelines and a systematic approach to the design for manufacturability of cast components. The system aids rapid generation and assessment of essential features in casting design to foresee manufacturing problems at the design stage itself. There is scope for similar analysis of other manufacture-driven design criteria and extension to new domains, particularly die casting and injection moulding. It is hoped that this will focus attention on the vast scope and augment inputs for further research in this area by both academics and practising engineers.

References

1. Bralla, J. G. *Handbook of product design for manufacturing*, 1988, McGraw–Hill.

2. Lewis, R. W., *et al.* Solidification in castings by finite element method, *Mater. Sci. Technol.*, 1990, **6**, 482–489.

3. LIN, H. J. AND HWANG, W. S. Three-dimensional fluid flow simulation for mould filling, *AFS Trans.*, 1988, **97**, 855–862.

4. PARK, J. C. AND LEE, K. Computer aided design of a pattern and risers for casting processes, *J. Engng Ind.*, 1991, **113**, 67–74.

Thesis Abstract (Ph.D.)

Effect of impurities and hard particles on the characteristics of dynamic recrystallization during hot working of aluminium and copper—A study using processing maps by N. Ravichandran

Research supervisor: Y. V. R. K. Prasad
Department: Metallurgy

1. Introduction

Dynamic recrystallization (DRX) imparts good workability during hot deformation of materials and its characteristics in face-centred cubic (fcc) metals are primarily influenced by the stacking fault energy (SFE). Earlier studies indicated that the low SFE metals like Cu undergo DRX and exhibit flow softening and oscillations in stress–strain curves. High SFE metals like Al show only dynamic recovery although DRX is reported in Al deformed to large strains. The aim of the present investigation is two fold: (1) to examine whether DRX occurs in Al and, if so, to study its characteristics, and (2) to study the effect of SFE on the characteristics of DRX with Cu as an example. In this study, emphasis has been placed on investigating the effects of impurities and hard particles on the DRX characteristics of Al and Cu. The strong influence of these factors on the static recrystallization (SRX) of these metals is well known. Earlier investigations followed a kinetic approach for analyzing the hot deformation behaviour. However, the interpretation of the apparent activation energy in terms of atomistic mechanisms was ambiguous. In the present study, a newer approach of dynamic materials modelling[1] was therefore adopted. In this model, the instantaneous power dissipated through microstructural changes in the workpiece during hot deformation is evaluated using the strain rate sensitivity (m) of flow stress and compared with an ideal linear dissipator ($m = 1$). The efficiency of power dissipation given by $[2m/(m + 1)]$ is plotted as a function of temperature and strain rate to obtain a processing map. The map exhibits different domains within which particular microstructural mechanisms occur and the domain of DRX is established by correlating efficiency with the ductility, grain size variations and other microstructural features. The advantages of this approach in understanding the hot deformation behaviour is discussed in several reviews[2,3].

2. Experimental

Aluminium of five different purities, aluminium containing hard particles, OFHC copper with two different oxygen contents and ETP copper containing varying volume fractions of oxide particles were used in this investigation. Cylindrical specimens of about 10-mm diameter and 15-mm height were used for hot compression testing which was chosen for the evaluation of hot working characteristics. Testing was conducted in the temperature range 0.6–0.9 T_m and strain rate range 0.001–100 s^{-1}. On the basis of the flow stress data as a function of temperature, strain rate and strain, power dissipation maps were developed using computer software. The DRX domain in the maps was established using correlations described above, and the temperature and strain rate for the peak efficiency in the domain were evaluated.

3. Results and discussion

In the processing map for 99.999% Al, a domain of DRX is established and the temperature and strain rate corresponding to the efficiency peak is 375°C and 0.001 s^{-1}. The maximum efficiency of power dissipation for

DRX is about 55%. The DRX temperature increased with decrease in the purity of Al and is about 600°C for 99.5% Al. The DRX strain rate, however, remained unaffected. The presence of hard particles has shifted the DRX domain to higher strain rates (about 0.1 s^{-1}) and reduced the efficiency of power dissipation to about 35%. The results are explained on the basis of a simple DRX model which considers the rate of interface formation (nucleation of recrystallized grain boundary) *versus* rate of its migration. In Al (high SFE) the rate of nucleation is faster than the rate of migration which therefore controls DRX. The impurity atoms diffuse to grain boundary, lower its energy and reduce the rate of migration. Higher temperatures are therefore required for the occurrence of DRX. The particles have a drag effect on the grain boundary which migrates to shorter distances requiring smaller migration times. The DRX in this case is less efficient in dissipating power, occurs at higher strain rates and results in grain refinement. The results clearly show that DRX occurs in Al and its characteristics are essentially similar to those of static recrystallization, although DRX occurs at much high temperature[4].

The processing map for OFHC Cu (30 ppm oxygen) revealed a domain of DRX centred at 850°C and 100 s^{-1} with a peak efficiency of 35%. The DRX strain rate is lower at higher oxygen content, the effect being more significant when the oxygen content is higher than 150 ppm (present as oxide particles). The DRX temperature showed an initial decrease with oxygen content before rising steeply at higher oxygen contents. In Cu, being a low SFE metal, DRX is controlled by the rate of nucleation which is slower than the rate of migration. Oxygen when present both as an interstitial and as oxide particles increases the rate of dislocation generation and hence the rate of the DRX strain rate. The large back stress caused by the presence of oxide particles is responsible for the increase in DRX temperature[5].

4. Conclusion

In conclusion, the results on the processing maps for hot deformation revealed that DRX occurs in Al, and that impurities and hard particles increase the DRX temperature and strain rate, respectively. On the other hand, in Cu, the DRX strain rate as well as the DRX temperature are influenced by the interstitial oxygen and oxide particles. On the basis of a simple model, it is shown that DRX in high SFE metals (Al) is controlled by the rate of migration of grain boundaries while in low SFE metals (Cu) DRX is nucleation controlled[6].

References

1. PRASAD, Y. V. R. K., GEGEL, H. L., DORAIVELU, S. L., MALAS, J. C., MARGON, J. C., LARK, K. A. AND BARKER, D. R. — Modeling of dynamic behaviour in hot deformation: Forging of Ti6242, *Metall. Trans A*, 1984, **15**, 1883.

2. GEGEL, H. L., MALAS, J. C., DORAIVELU, S. M. AND SHENDE, V. A. — *Metal handbook*, Vol. 14, pp. 417–438, 1988, ASM.

3. ALEXANDER, J. M. — Modelling hot deformation of steels, pp. 101–114, 1989, Springer–Verelg.

4. RAVICHANDRAN, N. AND PRASAD, Y. V. R. K. — Dynamic recrystallization during hot deformation of aluminium: A study using processing maps, *Metall. Trans. A*, 1991, **22**, 2339–2348.

5. RAVICHANDRAN, N. AND PRASAD, Y. V. R. K. — Influence of dynamic recrystallization during hot working of polycrystalline copper, *Mater. Sci. Engng A*, 1992, **156**, 195–203.

6. PRASAD, Y. V. R. K. AND RAVICHANDRAN, N. — Effect of stacking fault energy on the dynamic recrystallization during hot working of F.C.C. metals: A study using processing maps, *Bull. Mater. Sci.*, 1991, **14**, 1241–1248.

Thesis Abstract (M.Sc. (Engng))

A neuromorphic solution to the inverse kinematic problem of serial manipulators

by Sukumar Bhattacharya

Research supervisor: Asitava Ghosal
Department: Mechanical Engineering

1. Introduction

A serial manipulator is a chain of rigid numbers or links, connected by joints, with one end fixed and the other free. The free end has an end-effector attached to it for the performance of various tasks.

If C^n represents the joint space of the manipulator and T^m, the task space of the manipulator, then the forward kinematics can be represented as a continuous differentiable nonlinear vector function, $\mathbf{f} : C^n \rightarrow T^m$. The inverse kinematics problem is: given the position and orientation of the end-effector, $\mathbf{x} \in T^m$ and the link parameters, to find joint-displacements, $\mathbf{q} \in C^n$. The *inverse kinematic* problem is difficult to solve. Closed-form solutions exist only for certain classes of manipulators[1]. Iterative methods give only one solution of the many possible in one iteration cycle. For redundant manipulators, with $n > m$, there are in general infinitely many solutions and pseudoinverse of the manipulator Jocobian matrix is used to choose one among the infinity of solutions. Additional effort is often required to obtain solutions which avoid obstacles, singularities and do not violate joint limits.

We propose a neural architecture to solve the inverse kinematics problem for serial manipulators. The proposed neural architecture concurrently generates a configuration space trajectory for a given task space trajectory, and automatically eliminates solutions that violate joint limits.

2. Laterally inhibited neural field

The dynamic properties of an n-dimensional laterally inhibited neural field[2] have been derived. These properties are used in the kinematics of our neural architecture. Lateral interactions are through connections (or weights) of the following type:

- Excitatory connections between proximate neurons.
- Inhibitory connections between distant neurons.
- The connections are symmetric.
- The field is homogeneous.

The following are consequences of dynamic properties of such a laterally inhibited field:

- The field can retain a stable localized excitation of size R even in the absence of stimulus.
- Such a local excitation moves only if stimulus at its boundary is unbalanced.
- If the local excitation moves then it comes to stop at a peak around which the stimulus is balanced.

3. Neural architecture for inverse kinematics

The architecture consists of three networks (Fig. 1).

- The *Task space map* is an m-dimensional network which forms a representation of the m-dimensional task space through self-organization based on Kohonen's algorithm[3].
- The *Configuration map* is an n-dimensional network representing the joint space of the manipulator, where n is the dimension of the joint space. This network also self-organizes using the Kohonen algorithm.

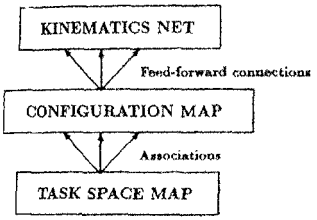

Fig. 1. Neural architecture for inverse kinematics.

- The *Kinematics net* is isomorphic to the configuration map. However, it is a laterally inhibited network which has the dynamics described in the previous section: This network retains an excitation permanently. The position of the center of this excitation codes the configuration of the manipulator at all times. Therefore, further in this work, we refer to the center of this excitation as the 'current configuration'.

An active neuron *C in the configuration* map (neuron K at $\mathbf{x}_k$ in the kinematics net is its corresponding neuron) through feedforward connections supplies a stimulus at y in the kinematics net, which is given by

$$S(\mathbf{y}, C) = \begin{cases} S_0\left(1 - \frac{|\mathbf{x}_k - \mathbf{y}|}{r_0}\right) & \text{if } |\mathbf{x}_k - \mathbf{y}| < r_0 \\ 0 & \text{otherwise} \end{cases} \quad (1)$$

Learning in this architecture consists of two stages:

- Self-organisation of the task space map and the configuration map.
- As configurations are sampled at random, active neurons coding the task space position and configuration in the respective maps get associated.

During operation, the task space trajectory that the end-effector must follow gets manifested on the task space map as a sequence of adjacent active neurons. As a neuron becomes active on the task space map, it makes active several neurons, which are associated with the active task space neuron, on the configuration map. These active neurons create stimulus on the kinematics net which makes the current configuration move. The trajectory of this motion gives the configuration trajectory.

4. Results

4.1. *Simulation*

We have carried out simulations of this architecture for planar nonredundant (2R) and planar redundant (3R) manipulators. The programs have been written in C on a IRIS-4D workstation. The trajectory is input with a mouse. The details are as follows:

Type	*Task space map*	*Configuration map*	*Link lengths*	*Joint limits*
2R	100×100 network	50×50 network	$l_1 = l_2 = 2$	$\theta_1, \theta_2 \in \left[-\frac{\pi}{2}, \frac{\pi}{2}\right]$
3R	100×100 network	$30 \times 30 \times 30$ network	$l_1 = 2\ l_2 = l_3 = 1$	$\theta_1, \theta_3 \in \left[0, \frac{\pi}{2}\right] \theta_2 \in \left[-\frac{\pi}{4}, \frac{\pi}{4}\right]$

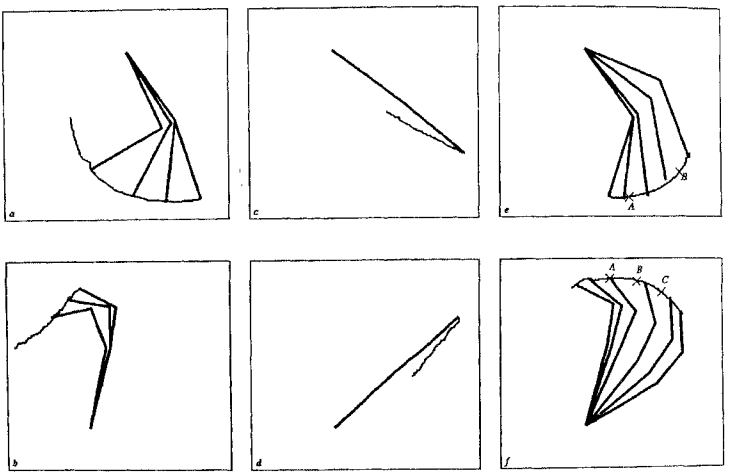

Fig. 2. Simulation results.

Figures 2a and b show that joining limits are not violated during tracking. Figures 2c and d show that at singular configurations tracking does not take place in directions that require unbounded joint speeds. Figures 2e and f show cross marks labelled A, B, etc., at a few places along the trajectory being tracked. Table I shows the errors according to the labels.

Table I

Manipulator	*Location*	*x-error*	*y-error*
2R	A	0.0358	−0.0148
	B	−0.0143	0.095
3R	A	−0.0487	−0.017
	B	−0.0263	0.0262
	C	−0.101	0.0126

4.2. *Analysis*

The learning and operation in this architecture have been analysed mathematically. The following are the main results.

- 'Current configuration' is always defined.
- Joint limits are never violated in tracking.
- At singular configurations, no tracking in certain directions.
- Operation has all desirable characteristics of an inverse kinematic algorithm.

1. No unbounded joint speeds during tracking.
2. Choice of only one of the inverse solutions.
3. The inverse solution is unique.
4. Solution is time invariant.

References

1. CRAIG, J. J. *Introduction to robotic mechanisms and control*, 1989, Addison–Wesley.
2. SHUN-ICHI AMARI Dynamics of pattern formation in lateral-inhibition type neural fields, *Biol. Cybern.*, 1977, 27, 77 87.
3. KOHONEN, T. Self-organized formation of topologically correct feature maps, *Bio. Cybern.*, 1982, 43, 59 69.